

1 Geostationary observations of atmospheric ammonia over East Asia: 2 spatio-temporal variations revealed by three years of FY-4B/GIIRS 3 measurements

4 Mengya Sheng¹, Runyi Zhou¹, Jiancong Hua¹, Shan Han¹, Shangyi Liu¹, Lin Zhang², Wei Wang³, Ruijun
5 Dang⁴, Hansen Cao⁵, Zichong Chen⁶, Yixuan Gu⁷, Mingxu Liu⁸, Lu Lee⁹, Chengli Qi⁹, Feng Lu⁹,
6 Changpei Han¹⁰, Mark W. Shephard¹¹, Nadir Guendouz¹², Camille Viatte¹², Lieven Clarisse¹³, Martin
7 Van Damme^{13,14}, Cathy Clerbaux^{12,13}, Zhao-Cheng Zeng^{1,*}

8 ¹ School of Earth and Space Sciences, Peking University, Beijing 100871, China

9 ² Laboratory for Climate and Ocean-Atmosphere Studies, Department of Atmospheric and Oceanic Sciences, School of Physics,
10 Peking University, Beijing 100871, China

11 ³ Key Laboratory of Environmental Optics and Technology, Anhui Institute of Optics and Fine Mechanics, Chinese Academy
12 of Sciences, Hefei 230031, China

13 ⁴ School of Engineering and Applied Sciences, Harvard University, Cambridge, MA 02138, USA

14 ⁵ School of Environmental Science and Engineering, Southern University of Science and Technology, Shenzhen, Guangdong
15 518055, China

16 ⁶ Hong Kong University of Science and Technology, Guangzhou 511400, China

17 ⁷ Jiangsu Key Laboratory of Atmospheric Environment Monitoring and Pollution Control, Collaborative Innovation Center of
18 Atmospheric Environment and Equipment Technology, Joint International Research Laboratory of Climate and Environment
19 Change, School of Environmental Science and Engineering, Nanjing University of Information Science and Technology,
20 Nanjing 210044, China

21 ⁸ College of Environmental Sciences and Engineering, Peking University, Beijing 100871, China

22 ⁹ Key Laboratory of Radiometric Calibration and Validation for Environmental Satellites, National Satellite Meteorological
23 Center, China Meteorological Administration, Beijing 100081, China

24 ¹⁰ Key Laboratory of Infrared Science and Technology, Shanghai Institute of Technical Physics, Chinese Academy of Sciences,
25 Shanghai 200083, China

26 ¹¹ Environment and Climate Change Canada, Toronto, Ontario M3H 5T4, Canada

27 ¹² LATMOS/IPSL, Sorbonne Université, UVSQ, CNRS, Paris 75252, France

28 ¹³ Spectroscopy, Quantum Chemistry and Atmospheric Remote Sensing (SQUARES), Brussels Laboratory of the Universe
29 (BLU-ULB), Université libre de Bruxelles (ULB), Brussels 1050, Belgium

30 ¹⁴ Royal Belgian Institute for Space Aeronomy, Brussels 1180, Belgium

31 *Correspondence to: Zhao-Cheng Zeng (zczeng@pku.edu.cn)*

32 **Abstract.** Satellite observations play a crucial role in quantifying ammonia sources by capturing large-scale variations of
33 atmospheric NH₃ concentrations. As the world's first geostationary hyperspectral infrared sounder, the Geostationary
34 Interferometric Infrared Sounder (GIIRS) on board China's FengYun-4 satellite series provides a unique opportunity to
35 monitor the diurnal cycle of NH₃. Using NH₃ retrievals from July 2022 to June 2025, this study investigates the spatio-temporal
36 variability of NH₃ columns over East Asia, with a focus on daytime variations (07:00–19:00 local time) in major agricultural
37 regions. Inter-comparison with polar-orbiting IASI and CrIS data shows that GIIRS NH₃ retrievals are consistent in capturing
38 spatial patterns and temporal dynamics. The NH₃ peaks occur between March and July, with peak timing earlier in the south

39 and later in the north, reflecting regional differences primarily driven by agricultural activities. Validation with ground-based
40 FTIR measurements at Hefei in eastern China demonstrates the accuracy of GIIRS NH₃, with a correlation coefficient of 0.77
41 and an RMSE of 9.67×10^{15} molec/cm², while reproducing daytime variations observed by FTIR. For major agricultural areas,
42 the NH₃ columns generally increase from early morning to late afternoon, reaching 1.10–1.56 times morning levels in summer
43 and spring. Compared with GEOS-CF model simulations, the results reveal pronounced discrepancies in spatial distributions
44 over the Sichuan Basin in southwestern China and daytime variations over northern India. These findings highlight the valuable
45 capability of FY-4B/GIIRS in identifying and tracking daytime dynamics of NH₃ sources over East Asia, offering new insights
46 beyond current low-Earth orbit (LEO) instruments.

47 **1 Introduction**

48 Gaseous ammonia (NH₃), the most abundant alkaline gas and a major reactive nitrogen compound in the atmosphere,
49 plays a critical role in the global nitrogen cycle. NH₃ is an important precursor of secondary inorganic aerosols. It rapidly
50 reacts with atmospheric acids such as sulfuric acid (H₂SO₄) and nitric acid (HNO₃) to form ammonium sulfate ((NH₄)₂SO₄)
51 and ammonium nitrate (NH₄NO₃) (Seinfeld et al., 2016). These ammonium-containing aerosols are the primary components
52 of fine particulate matter (PM_{2.5}) and have been identified as key contributors to elevated PM_{2.5} concentrations and haze
53 pollution in both rural areas (Jang et al., 2025; Saraswati et al., 2019; Meng Z. et al., 2018) and megacities (Lin et al., 2020)
54 in Asia, posing significant threats to air quality, visibility, and public health. NH₃ also exerts indirect influences on global
55 climate change, for example, by driving nitrous oxide (N₂O) formation via atmospheric oxidation (Pai et al., 2021) and by
56 altering radiative forcing through aerosol-mediated processes (Gong et al., 2024). Moreover, excessive emissions and
57 deposition of NH₃ have adverse effects on ecosystems, causing biodiversity loss, soil acidification, and water eutrophication
58 (Bobbink et al., 2010). Anthropogenic NH₃ emissions primarily originate from agricultural activities, particularly from
59 synthetic fertilizer application and livestock farming, with additional contributions from industrial processes and transportation
60 (Behera et al., 2013). Numerous studies have indicated that a relatively strong reduction in PM_{2.5} and N₂O levels can be
61 achieved by decreasing agricultural emissions (e.g., Luo et al., 2025). Therefore, comprehensive quantification and
62 understanding of NH₃ emission sources are essential for developing effective air quality and climate mitigation strategies.

63 Asia is the world's most significant NH₃ emission region, accounting for over 30% of global NH₃ emissions annually as
64 reported by the Emissions Database for Global Atmospheric Research (EDGAR) inventory. Due to widespread use of urea-
65 based nitrogen fertilizers and high livestock densities, cropland areas such as the Indo-Gangetic Plain in India and the North
66 China Plain in China are recognized as major global NH₃ emission hot spots (Van Damme et al., 2018). NH₃ volatilization is
67 strongly controlled by surface conditions, including temperature and moisture, and irrigation-driven NH₄⁺ accumulation in
68 soils (Behera et al., 2013). The resulting atmospheric NH₃ concentrations over a region are further influenced by meteorology-
69 and topography-induced constraints on atmospheric mixing and transport, chemical reactions dependent on the concentrations
70 of reactive acidic gases, and dry and wet deposition (Dammers et al., 2017a). In most regions, NH₃ concentrations in summer

71 are significantly higher than those in winter, driven by emissions from urea hydrolysis and livestock manure decomposition
72 (Warner et al., 2016; Van Damme et al., 2015). Given its short atmospheric lifetime of a few hours to several days, NH₃ exhibits
73 large intra-day variability in concentration from both agricultural and non-agricultural sources. Several studies have employed
74 surface measurements to investigate the diurnal variability of NH₃ and its controlling mechanisms, revealing that diurnal
75 patterns in urban and rural areas differ markedly across seasons (Gu et al., 2022; He et al., 2020; Chang et al., 2019; Huy et
76 al., 2017; Meng Z. et al., 2011). These analyses are limited by the sparse spatial coverage and short temporal duration of
77 ground-based monitoring networks. To complement observations, atmospheric chemistry models have been applied to simulate
78 NH₃ at regional and global scales, and refinements in surface exchange schemes have improved NH₃ modeling (Jongenelen et
79 al., 2025; Cao et al., 2022). However, the mechanisms underlying the diurnal variability of atmospheric NH₃ in different
80 emission regions still remain poorly understood.

81 Satellite observations facilitate top-down inversion methods for monitoring NH₃ variations across multiple spatial scales.
82 The hyperspectral infrared sounders onboard polar-orbiting satellites in low-Earth orbit (LEO), such as the Infrared
83 Atmospheric Sounding Interferometer (IASI; Clarisse et al., 2009), the Tropospheric Emission Spectrometer (TES; Beer et al.,
84 2008), the Atmospheric Infrared Sounder (AIRS; Warner et al., 2016), the Cross-track Infrared Sounder (CrIS; Shephard et al.,
85 2020), and the Hyperspectral Infrared Atmospheric Sounder (HIRAS; Hua et al., 2026), have provided global monitoring of
86 atmospheric NH₃ column densities. Satellite-based NH₃ retrievals have been widely used to investigate the spatial distribution
87 of NH₃ emission sources (e.g., Van Damme et al., 2018), to characterize spatiotemporal variations in atmospheric NH₃
88 concentrations (e.g., Van Damme et al., 2021; Shephard et al., 2020), and to constrain emission estimates (e.g., Cao et al., 2020;
89 Dammers et al., 2019) and dry deposition estimates (e.g., Kharol et al., 2018). Van Damme et al. (2021) reported that NH₃
90 concentrations increased from 2008 to 2018 in major agricultural regions globally, including South Asia, China, the United
91 States and some parts of Europe. Based on multi-year NH₃ maps, Van Damme et al. (2018) and Clarisse et al. (2019) identified
92 and quantified major industrial and agricultural NH₃ point sources, revealing that NH₃ emissions from approximately two-
93 thirds of these sources were underestimated by at least one order of magnitude in the EDGAR emission inventory. In addition,
94 NH₃ emission estimates based on satellite observations and inverse modeling indicated that bottom-up emission inventories
95 underestimate NH₃ emissions, especially during summer (e.g., Xu et al., 2023; Marais et al., 2021; Zhang et al., 2018).

96 Accurately monitoring the daily dynamics of NH₃ emissions imposes high sampling requirements in time and space on
97 atmospheric NH₃ measurements. Polar-orbiting satellites typically measure a given location at most twice per day. For example,
98 IASI and CrIS cross the equator at 09:30/21:30 and 01:30/13:30 local solar time (LST), respectively (Whitburn et al., 2016;
99 Shephard et al., 2015). The above satellite-based studies mostly used morning observations from IASI and afternoon
100 observations from CrIS, because of the lower uncertainties associated with a more favorable thermal state of the atmosphere
101 for the remote sensing of its lowest layers. Investigations of the spatial and temporal variability of NH₃ are constrained by the
102 limited coverage of satellite overpasses, leading to potential temporal representativeness biases and substantial uncertainties
103 in daily NH₃ emission estimates (Clarisse et al., 2019; Van Damme et al., 2018). The Geostationary Interferometric Infrared
104 Sounder (GIIRS) onboard the FY-4 series is the world's first hyperspectral infrared sounder in geostationary (GEO) orbit. It

105 was first launched as an experimental instrument on FY-4A in December 2016 and subsequently deployed as operational
106 instruments with enhanced sensitivity on FY-4B in June 2021 (Yang et al., 2017) and on FY-4C in December 2025. Compared
107 with current LEO instruments, GIIRS provides continuous day-and-night monitoring of atmospheric NH₃ over East Asia at
108 hourly-scale temporal resolution, representing a breakthrough in monitoring the diurnal cycle of atmospheric NH₃ variations
109 (Clarisse et al., 2021; Zeng et al., 2023a). Similarly, the Meteosat Third Generation sounding satellite (MTG-S1), launched in
110 July 2025, carries the Infrared Sounder (IRS), another geostationary hyperspectral infrared instrument designed to provide
111 higher spatio-temporal resolution observations (every 30 minutes) over Europe (Holmlund et al., 2021). A recent study by
112 Guendouz et al. (2025) investigated the correlation between GIIRS NH₃ and surface skin temperature and showed the potential
113 of discriminating sources between temperature-driven livestock/fertilizer volatilization and urea fertilizer application.

114 With over three years of FY-4B/GIIRS geostationary observations available from July 2022 to June 2025, unprecedented
115 opportunities have emerged to monitor the spatial and temporal variations of NH₃ concentrations and their evolution
116 throughout the day over East Asia. In this study, we highlighted the enhanced capability of GIIRS observations to identify
117 emission sources and capture daytime variations associated with agricultural activities, surpassing those reported by polar-
118 orbiting satellites. The data and methodology are described in Sect. 2. The spatial patterns and seasonal cycles of NH₃ observed
119 by GIIRS are compared with observations from IASI and CrIS, as well as estimates from the mosaic Asian anthropogenic
120 emission inventory (MIX) in Sect. 3.1. The data accuracy and temporal variations of satellite-derived NH₃ are validated against
121 ground-based Fourier Transform Infrared (FTIR) measurements at the Hefei station in Sect. 3.2. The daytime variations of
122 NH₃ from GIIRS observations and model simulations in major agricultural regions are discussed in Sect. 3.3. Conclusions are
123 summarized in Sect. 4.

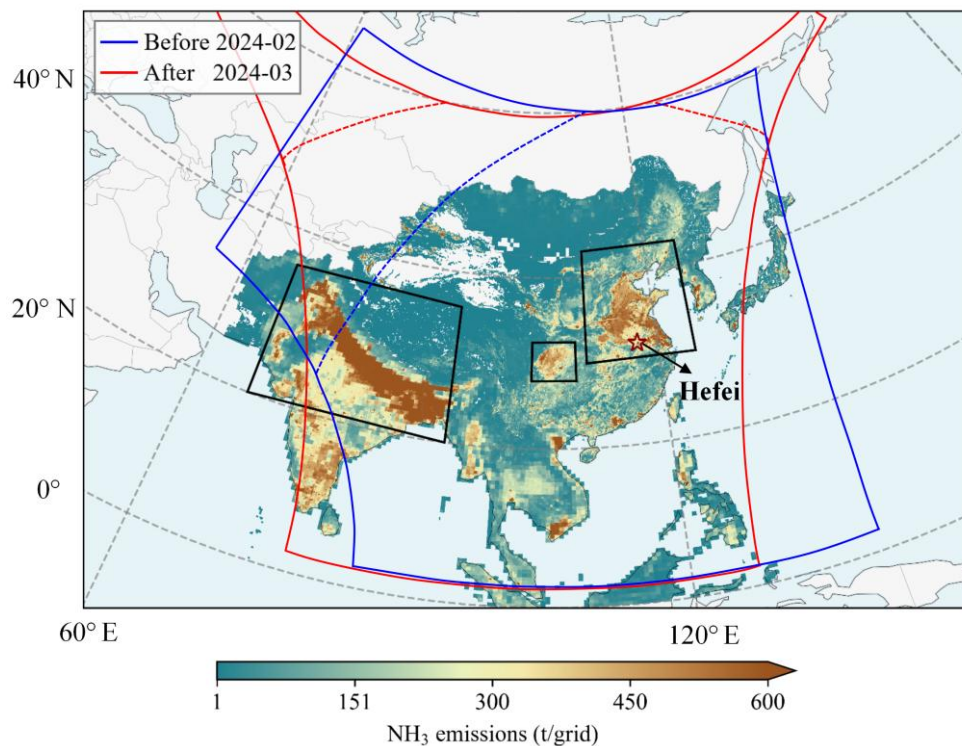
124 **2 Data and Methodology**

125 **2.1 Satellite NH₃ retrievals**

126 **2.1.1 GIIRS observations**

127 FY-4B/GIIRS was successfully launched on 3 June 2021 and began operating at 133°E on 11 April 2022, providing
128 observational data from 1 June 2022. As the FY-4A satellite approached fuel depletion, FY-4B was maneuvered from 133°E
129 to 105°E between 1 February and 5 March 2024 to take over FY-4A's observation duties, with measurements temporarily
130 suspended during this period. Since then, FY-4B/GIIRS has been operating nominally at 105°E. FY-4B/GIIRS observations
131 primarily cover the regions from 3°N to 55°N and 60°E to 137°E, encompassing East Asia and parts of South and Southeast
132 Asia (Fig. 1). The instrument performs measurements over the target region every 2 hours using a “step-stare” scanning mode.
133 Observations are conducted along 12 scanning lines from north to south, with 27 fields of regard (FORs) arranged from west
134 to east along each line. The FOR is a two-dimensional infrared detector array composed of 16 × 8 sparsely arranged pixels.
135 Each pixel has a nadir-projected size of approximately 12 km × 12 km, with a spacing of 12 km in both along-track and cross-

136 track directions between adjacent pixels. Initially, 12 measurement cycles in a day started at 00:00, 02:00, 04:00, ..., 22:00
137 UTC. After 6 September 2022, the start times were changed to 01:00, 03:00, 05:00, ..., 23:00 UTC, respectively.



138

139 **Figure 1. Spatial domain of FY-4B/GIIRS observations and NH₃ retrievals over East Asia. Blue and red solid lines outline GIIRS**
140 **observational coverage before and after the FY-4B orbital relocation, respectively. Blue and red dashed lines denote the**
141 **corresponding NH₃ retrieval domains, with viewing zenith angles greater than 70° excluded. The background map shows total**
142 **anthropogenic NH₃ emissions in 2017 from the MIXv2 emission inventory at a 0.1° grid resolution (Li et al., 2024). The red**
143 **pentagram marks the location of the Hefei station, which is further described in Sect. 3.2. Black boxes outline major agricultural**
144 **areas, including the North-Northeast China Plain, the Sichuan Basin, and the Indo-Gangetic Plain.**

145 Three years of NH₃ columns from July 2022 to June 2025 are retrieved from FY-4B/GIIRS spectra using the FengYun
146 Geostationary satellite Atmospheric Infrared Retrieval (FY-GeoAIR) algorithm, which exploits the strong NH₃ absorption
147 features in the 955–975 cm⁻¹ spectral region. FY-GeoAIR is a full-physics retrieval algorithm that integrates a forward radiative
148 transfer model for simulating upwelling thermal radiation and an optimal estimation-based inverse model for retrieving trace
149 gases and auxiliary parameters from the observed spectra (Zeng et al., 2023b). In this study, the retrieval configuration and
150 parameters are identical to those described in Zeng et al. (2023a), except that a profile-scaling retrieval approach was adopted
151 instead of the full-profile retrieval method. The full-profile retrieval method fully resolves the ammonia profile as 11 separate
152 layers. In contrast, the profile-scaling retrieval approach only retrieves the total column of NH₃. It applies a single
153 representative a priori profile (identical for all scenes) and scales this profile in the retrieval algorithm to optimize the spectra
154 fitting. In this case, there is only one state vector element for NH₃, instead of 11. The reasons for this change of the retrieval

155 configuration are: (1) the degrees of freedom for signal (DOFS) for most NH₃ retrievals as shown in Zeng et al. (2023a) is less
156 than one, indicating less than one piece of information is available from the spectra for NH₃ and not sufficient to constrain its
157 vertical distribution; (2) using the profile-scaling retrieval approach speeds up the retrieval calculation. Similarly, only total
158 column is retrieved for the interference gas H₂O. The retrieval yields the NH₃ column and the posteriori error estimate. In
159 addition, the column averaging kernel (AVK) is derived simultaneously in the optimal estimation framework. The column
160 AVK value at a given atmospheric layer represents the change in the retrieved total NH₃ column with respect to a perturbation
161 of the partial NH₃ column at that layer. It therefore reflects the height-dependent sensitivity determined by the temperature
162 difference between the surface and the given atmospheric layer (Fig. A1 and Fig. S1). This definition of AVK is similar to that
163 from the Total Carbon Column Observing Network (Wunch et al., 2011) and IASI (Clarisse et al., 2023), but differs from
164 conventional matrix AVK from optimal estimation (Shephard et al., 2011, 2015). Further details on interpretation and
165 calculation of the column AVK are provided in the Appendix.

166 In the NH₃ retrievals, regions with viewing zenith angles greater than 70° are excluded from the retrieval algorithm, as
167 large zenith angles increase the atmospheric path length and scattering effects while reducing the signal-to-noise ratio and
168 retrieval reliability. Observations that are cloud-contaminated or fail to converge within 10 iterations are also removed. To
169 obtain high-quality GIRS NH₃ observations, we also applied the following filtering criteria: (1) a root mean square error
170 (RMSE) of the fitting residual less than 0.2 K; (2) a reduced χ^2 less than 5; (3) retrieval error below 300%; (4) the absolute
171 difference between the a priori and retrieved surface skin temperature less than 10 K; (5) the bottom layer of column AVK
172 greater than 0.1; (6) the thermal contrast (TC) greater than 0 K; (7) the retrieved NH₃ columns are positive. The retrieval error
173 was calculated as the square root of the diagonal elements of the retrieval error covariance matrix for NH₃, normalized by the
174 ratio of the retrieved NH₃ column to the a priori NH₃ column. The TC is defined as the temperature difference between the
175 surface and the lowest atmospheric layer. The strict quality filtering results in large data gaps over the Tibetan Plateau
176 throughout the day, and over southern regions of China and India during 17:00–19:00 LST, where retrievals are frequently
177 discarded due to low sensitivity or cloud screening.

178 In this study, NH₃ retrievals from individual observations over land during daytime (7:00–19:00 LST) were utilized to
179 investigate spatial and temporal variations over East Asia (Fig. 2), whereas nighttime data were excluded due to insufficient
180 thermal contrast. To facilitate regional analysis, individual retrievals were averaged onto a 0.5° × 0.5° grid. For the analysis of
181 daytime NH₃ variations in Sect. 3.3, we further filtered the daytime observations by requiring TC > 5 K to ensure sufficient
182 sensitivity to near-surface NH₃. Figure S2 shows the number of data points before and after applying the TC > 5 K filtering
183 criterion. The fractions of valid observations remaining in the North-Northeast China Plain, the Sichuan Basin, and the Indo-
184 Gangetic Plain (as shown in Fig. 1) are about 83 %, 88 %, and 73 %, respectively.

185 2.1.2 IASI observations

186 The IASI instrument, jointly developed by the Centre National d'Études Spatiales (CNES) and the European Organisation
187 for the Exploitation of Meteorological Satellites (EUMETSAT), was specifically designed for deployment aboard the Metop

188 series satellites. Three identical instruments were successively onboard Metop-A, Metop-B and Metop-C platforms, launched
189 in 2006, 2012, and 2018, respectively. IASI operates in a sun-synchronous LEO at an altitude of approximately 800 km, with
190 a ground swath of ~2100 km and a spatial resolution of 12 km at nadir. It measures the Earth's emitted infrared radiation across
191 a spectral range of 645–2760 cm^{-1} with an apodized resolution of 0.5 cm^{-1} (Clerbaux et al., 2009). The near-real-time NH_3
192 dataset is retrieved using the Artificial Neural Network for IASI (ANNI) framework. This method converts the hyperspectral
193 signature of NH_3 , quantified by the so-called hyperspectral range index (HRI), into total column amounts (Whitburn et al.,
194 2016). Two independent validation studies demonstrated that IASI-retrieved NH_3 columns show good consistency with both
195 in situ and FTIR observations, exhibiting near-unity regression slopes and moderate biases (Guo et al., 2021; Wang et al.,
196 2020). In this study, we utilized NH_3 data from IASI observations on the Metop-B and Metop-C platforms from January 2017
197 to June 2025 for comparison with GIIRS observations. The data products provide total NH_3 columns derived from the ANNI
198 version 4 algorithm, which is about 15–20% larger than the previous version 3 due to the improved setup of HRI, but show
199 very similar NH_3 distribution (Clarisse et al., 2023). Here, NH_3 columns marked as recommended by both pre-filter and post-
200 retrieval quality flags in the data products were selected and then regridded onto a 0.5° spatial grid using arithmetic averaging.
201 The quality flags allow some negative columns to be retained, as discussed by Clarisse et al. (2019) and Whitburn et al. (2016).

202 **2.1.3 CrIS observations**

203 The Cross-track Infrared Sounder (CrIS) is a Fourier transform spectrometer (FTS) jointly developed by the National
204 Oceanic and Atmospheric Administration (NOAA) and the National Aeronautics and Space Administration (NASA), which
205 provides hyperspectral infrared measurements at a spectral resolution of 0.625 cm^{-1} with a nadir spatial resolution of ~14 km.
206 CrIS was first launched on the Suomi National Polar-orbiting Partnership (S-NPP) satellite on 28 October 2011 and
207 subsequently deployed on NOAA-20 (JPSS-1) on 29 November 2017 and on JPSS-2 on 10 November 2022. The NH_3 retrievals
208 from CrIS observations on S-NPP and NOAA-20 have been generated using the CrIS Fast Physical Retrieval (CFPR) algorithm
209 developed by Environment and Climate Change Canada (ECCC), which exploits spectral features near 967 cm^{-1} . A detailed
210 description of the CFPR algorithm can be found in Shephard et al. (2015, 2020). Independent validation studies against FTIR-
211 derived total column measurements have demonstrated that CFPR (version 1.3) shows good overall consistency, with a
212 correlation of approximately 0.8 and a slope of 1.02. For retrievals with total column values above 1×10^{16} molec/ cm^2 (ranging
213 from moderate to high levels), the relative bias is less than 5%. For smaller total column values ($< 1 \times 10^{16}$ molec/ cm^2), there
214 are larger differences, with CrIS retrievals about 30% higher than FTIR values (Dammers et al., 2017a). However, these
215 validations did not account for non-detects below the detection limit of the sensor ($\sim 4 \times 10^{15}$ molec/ cm^2 under typical remote
216 sensing conditions) (Shephard et al., 2025; White et al., 2023), which could reduce potential high-biases over non-source
217 conditions. In this study, we used CrIS NH_3 data product from NOAA-20 (version 1.6.4), spanning the period from March
218 2019 to April 2025. The product provides geolocation information, vertically integrated ammonia total columns, retrieval
219 uncertainties, quality flags, and additional metadata. The dataset utilizes the information content of the satellite measurements
220 to explicitly identify and account for cloud-free observations below the sensor detection level (White et al., 2023). Our analysis

221 focuses on NH₃ retrievals over land, characterized by land fraction > 0, quality flag ≥ 4, cloud flag ≠ 1, and DOFS ≥ 0.1.

222 **2.2 Ground-based FTIR measurements at Hefei**

223 The Hefei station (31.91°N, 117.17°E) is located in the northwestern rural area of Hefei city, China. The surrounding
224 region is part of a typical Jianghuai agricultural region, where wetlands and croplands are interspersed in a distinctive landscape
225 pattern. Since July 2015, a high-resolution ground-based Fourier transform infrared spectrometry (FTIR) has been operating
226 at the station to record mid-infrared (MIR) solar absorption spectra (700–4000 cm⁻¹) for the remote sensing of greenhouse
227 gases and trace species (Wang et al., 2017). A previous study has demonstrated that FTIR measurements at Hefei effectively
228 capture the spatiotemporal variability of NH₃ columns, and the retrievals are broadly consistent with IASI satellite data (Wang
229 et al., 2022). In this study, FTIR-derived NH₃ column data from 2017 to 2024 were averaged into hourly means and used for
230 the validation and cross-comparison of satellite-based NH₃ retrievals. It should be noted that the data primarily covers the
231 period from 8:00 to 17:00 LST, with limited available observations between 17:00 and 18:00 LST.

232 **2.3 NH₃ emission inventory**

233 The MIXv2 Asian emission inventory was developed under the framework of the Model Inter-Comparison Study for Asia
234 Phase IV (MICS-Asia IV) project by assembling a mosaic of up-to-date regional and national emission inventories (Li et al.,
235 2024). It provides monthly estimates of NH₃ emissions for 2010–2017 at a spatial resolution of 0.1° × 0.1° grid across seven
236 sectors. The inventory incorporated nine regional and two global emission inventories, covering 23 countries and regions in
237 East, Southeast and South Asia. Anthropogenic NH₃ emissions were based on the best available emission inventories, including
238 a process-based NH₃ emission inventory developed by Peking University (PKU-NH₃) for China, the official Japan emission
239 inventory (JPN), and the Clean Air Policy Support System (CAPSS) emissions for the Republic of Korea, and were gap-filled
240 with REAS version 3 for Asia (REASv3). Studies have suggested that the spatial distribution of NH₃ emissions in the inventory
241 is generally reliable, with differences compared to other emission inventories and satellite-constrained NH₃ emissions typically
242 within 20–50% (Luo et al., 2022; Zhang et al., 2019; Kang et al., 2016).

243 **2.4 Hourly NH₃ data from GEOS-CF model**

244 The Goddard Earth Observing System composition forecast (GEOS-CF) is a high-resolution global constituent prediction
245 model developed by NASA's GMAO. It expands on the GEOS weather and aerosol modeling system by introducing the GEOS-
246 Chem chemistry module, providing near-real-time, three-dimensional gridded information on atmospheric composition (Keller
247 et al., 2021). The emission inputs of anthropogenic NH₃ emissions used by GEOS-CF are mainly from the Hemispheric
248 Transport of Air Pollution emissions inventory (HTAP v2.2), which provides monthly data at a 0.1° spatial resolution. The
249 model runs at hourly intervals with 0.25° × 0.25° horizontal resolution and 72 hybrid-eta levels from the surface to 0.01 hPa. In
250 this study, NH₃ vertical profiles were obtained from 1-day replay simulations (referred to as “hindcast”) constrained by pre-

251 computed meteorological analysis fields, and NH₃ total columns were calculated by combining the model's vertical pressure
252 levels and surface pressures from the fifth-generation ECMWF reanalysis (ERA5) (Hersbach et al., 2023).

253 **2.5 The derivation of NH₃ variations**

254 **2.5.1. Curve-fitting Method for trend analysis**

255 To quantify the temporal changes in NH₃ columns, we applied a curve-fitting method to obtain daily time series of
256 satellite-based NH₃ observations. This method is widely used to extract temporal variation characteristics of atmospheric
257 composition, such as NH₃ (Wang et al., 2022; Van Damme et al., 2015). As shown in Eq. (1), it integrates a polynomial function
258 and a sum of harmonic function, representing long-term linear trend and seasonal cycles, respectively.

$$259 \quad f(t) = a_0 + a_1 t + \sum_{n=1}^4 (\beta_n \sin(2n\pi t) + \gamma_n \cos(2n\pi t)) \quad (1)$$

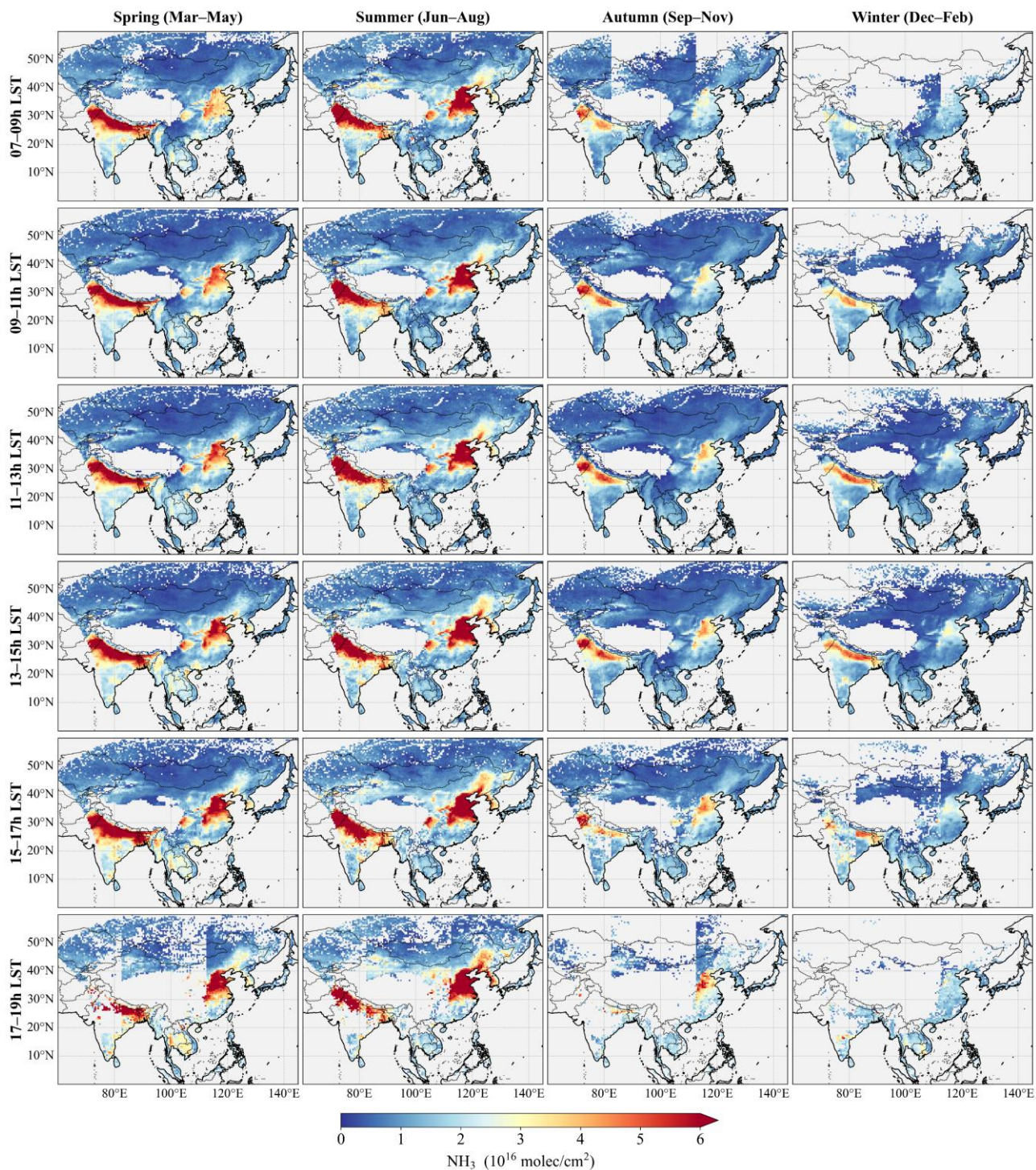
260 where f is the daily fitting result, t is the time in decimal years, the coefficients (a_0 , a_1 , β_n , γ_n) are determined by the least
261 squares regression. In Sect. 3.1, the fitting analysis was performed separately for each $0.5^\circ \times 0.5^\circ$ grid cell, with more than
262 500 data points and observation dates spanning over 100 days. Extreme values and minima of the fitted curves were then
263 calculated to identify temporal inflection points and determine the months with peak NH₃ concentrations.

264 **2.5.2. Gridded NH₃ enhancements**

265 Based on the spatial distribution of NH₃ emissions and concentrations, the study domain was divided into 14 subregions
266 (Fig. 6). Monthly variations of NH₃ columns for each subregion were obtained by aggregating the daily fitted values calculated
267 in Sect. 2.5.1, which represent the regional background levels. NH₃ anomalies from individual measurements were then
268 calculated by subtracting NH₃ backgrounds, as defined in Eq. (2).

$$269 \quad A_i = X_i - BK_{r,m} \quad (2)$$

270 where A_i is the NH₃ anomaly for the individual i -th retrieval, X_i is the observed NH₃ column, and $BK_{r,m}$ represents the NH₃
271 background for region r and month m corresponding to the spatial location and observation time of retrieval i . For each grid
272 cell, positive anomalies with occurrences of elevated concentrations ($> 1.0 \times 10^{16}$ molec/cm²) exceeding 30 days were classified
273 as NH₃ enhancements. The frequency of such occurrences, expressed as number of days, serves as a useful indicator of
274 enhanced emissions, such as recurring agricultural activities (Shephard et al., 2020; Warner et al., 2016).



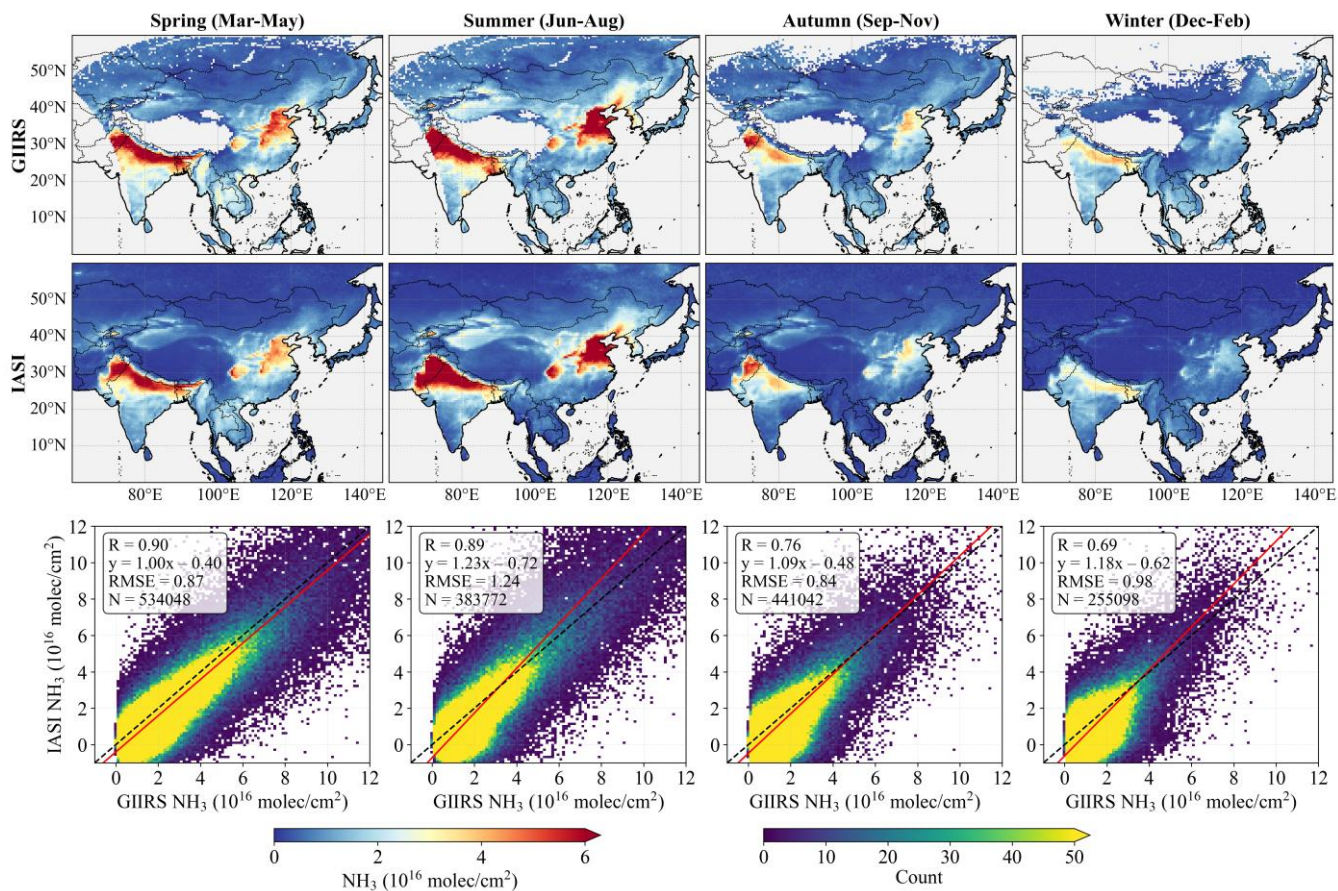
275
 276 **Figure 2. Seasonal maps of NH_3 columns from FY-4B/GHRS observations from July 2022 to June 2025 averaged for every 2 hours**
 277 **according to local solar time (LST) on a $0.5^\circ \times 0.5^\circ$ grid and for different seasons (spring: March-April-May; summer: June-July-**
 278 **August; autumn: September-October-November; winter: December-January-February).**

279 **3 Results and discussion**

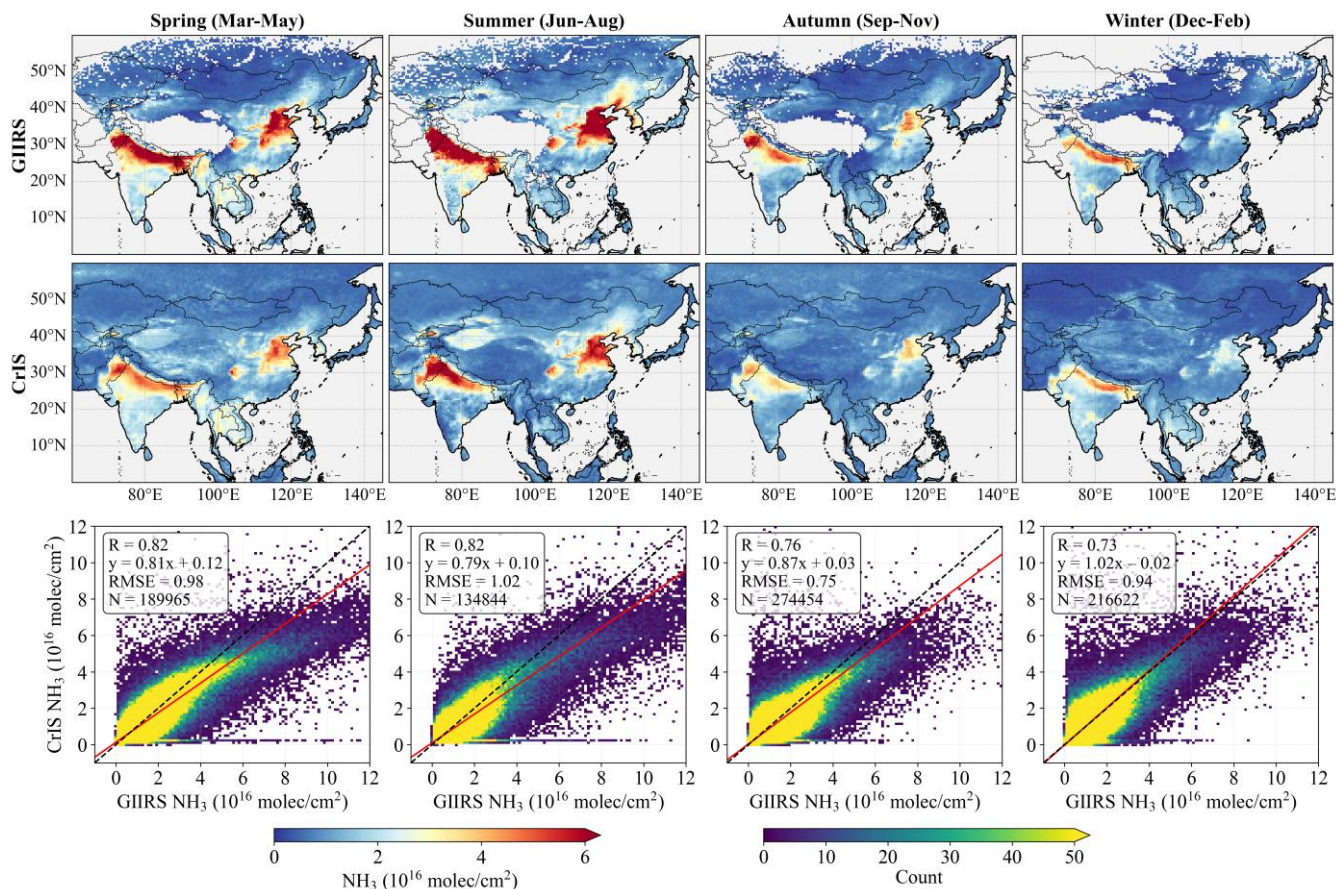
280 **3.1 Spatial and temporal NH₃ distribution over East Asia**

281 Figure 2 illustrates the three-year averaged seasonal NH₃ column concentrations retrieved from FY-4B/GIIRS
282 observations over East Asia from July 2022 to June 2025, presented on a 0.5°×0.5° grid at two-hour intervals. The observations
283 are aggregated according to local solar time (LST) to facilitate the analysis of NH₃ diurnal variations and consistent
284 comparisons. The study region spans multiple time zones and data availability during the 07:00–9:00 and 17:00–19:00 LST
285 periods is substantially reduced due to retrieval filtering, resulting in noticeable boundaries across longitudes. Elevated NH₃
286 columns, significantly above background levels, are observed over the Indo-Gangetic Plain, the North China Plain, the Sichuan
287 Basin, and the Northeast China Plain (as shown by the black boxes in Fig. 1). The daytime NH₃ columns reach values exceeding
288 4×10^{16} molec/cm², primarily driven by intensive agricultural activities and supplemented by non-negligible contributions from
289 urban and industrial emissions. Localized weaker enhancements of NH₃ column concentrations are evident over agricultural
290 core areas in China (including the Ningxia Irrigation Plain, the Wei River Plain, the Jiangnan Plain, and oasis agriculture in
291 the arid regions of Xinjiang), as well as the central Deccan Plateau in India, the Mekong Delta in Vietnam, the Chao Phraya
292 River Plain in Thailand, and the Fergana Valley in Uzbekistan (as shown by the dashed boxes in Fig. S4). Most of these regions
293 exhibit higher NH₃ columns in summer and considerable daytime variability, with large differences between morning and
294 afternoon observations. A detailed analysis of diurnal patterns over major source regions is provided in Sect. 3.3.

295 Comparisons with the spatial distribution of NH₃ columns observed by polar-orbiting infrared sounders of IASI and CrIS
296 show reasonable agreement, especially in regions with high NH₃ columns above 3×10^{16} molec/cm² (Fig. 3 and Fig. 4). The
297 seasonal increases in atmospheric NH₃ are most pronounced in spring and summer. Despite generally similar seasonal and
298 spatial patterns, inter-satellite NH₃ observations exhibit noticeable differences. Relative to the IASI observations, GIIRS
299 typically shows very small systematic differences with fitted slopes close to unity. In contrast, GIIRS observations tend to
300 show higher NH₃ columns than CrIS in most high-concentration regions, with mean differences of approximately 25–50%
301 relative to the corresponding GIIRS values in summer. The data point scattering in the comparison plots primarily results from
302 spectral noise. Overall, there is good agreement between GIIRS-derived NH₃ columns and those from IASI and CrIS across
303 different seasons.



304
 305 **Figure 3. Comparison of NH_3 columns observed by GHIRS and IASI during morning overpasses (~09:30 LST) from July 2022 to**
 306 **June 2025. Seasonal maps are presented on a $0.5^\circ \times 0.5^\circ$ grid. Scatter plots compare GHIRS and IASI data matched by overpass**
 307 **times within 1 hour and spatial locations within the same $0.5^\circ \times 0.5^\circ$ grid cells.**



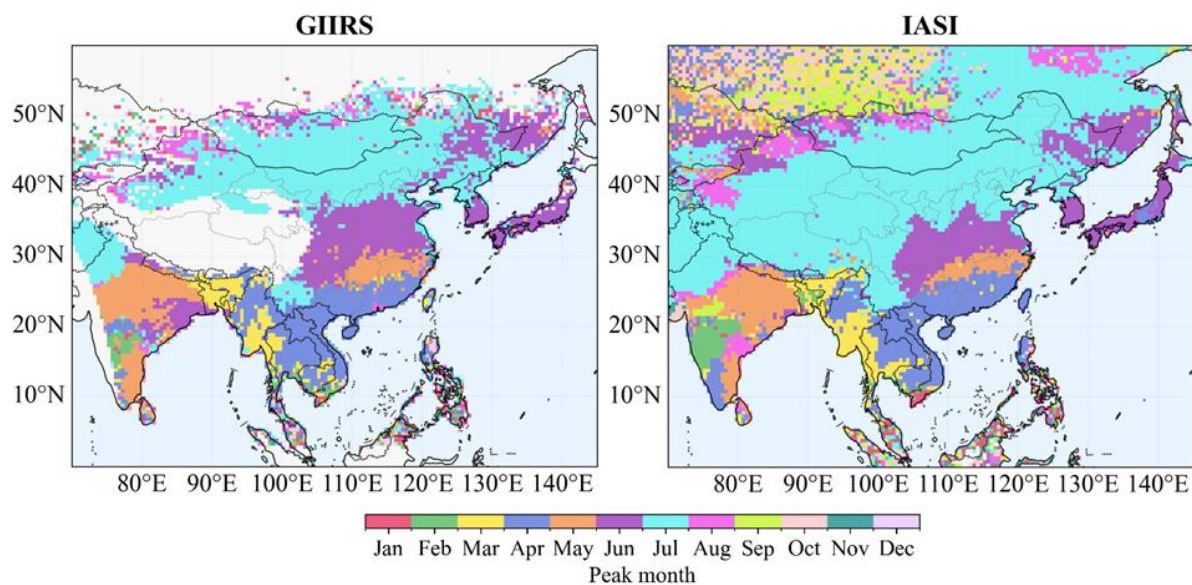
308
 309 **Figure 4. Comparison of NH₃ columns observed by GIIRS and CrIS during afternoon overpasses (~13:30 LST) from July 2022 to**
 310 **April 2025. Seasonal maps are presented on a 0.5° × 0.5° grid. Scatter plots compare GIIRS and CrIS data matched by overpass**
 311 **times within 1 hour and spatial locations within the same 0.5° × 0.5° grid cells.**

312 To account for the effects of differing vertical sensitivities, as reflected by the AVKs, and a priori profiles among these
 313 satellites (see Fig. S1 for example), we conducted experiments using model profile data and satellite AVKs over the North-
 314 Northeast China Plain (30°–43°N, 110°–125°E) in June 2024 (Text S1). Model simulations of NH₃ profiles were convolved
 315 with different satellite AVKs to generate AVK-smoothed NH₃ columns, representing the NH₃ columns that a certain satellite
 316 would retrieve if the model simulations were the “truth”. We then compared AVK-smoothed NH₃ column datasets generated
 317 using different satellite AVKs to evaluate the effects of different satellite vertical sensitivities. The comparison results (Fig. S5)
 318 show high correlations ($R > 0.9$) and slopes close to unity. This indicates consistency in the detection of NH₃ across different
 319 sensors, and that the effects of different AVKs and a priori profiles are small in terms of total column retrieval when comparing
 320 different satellite retrievals.

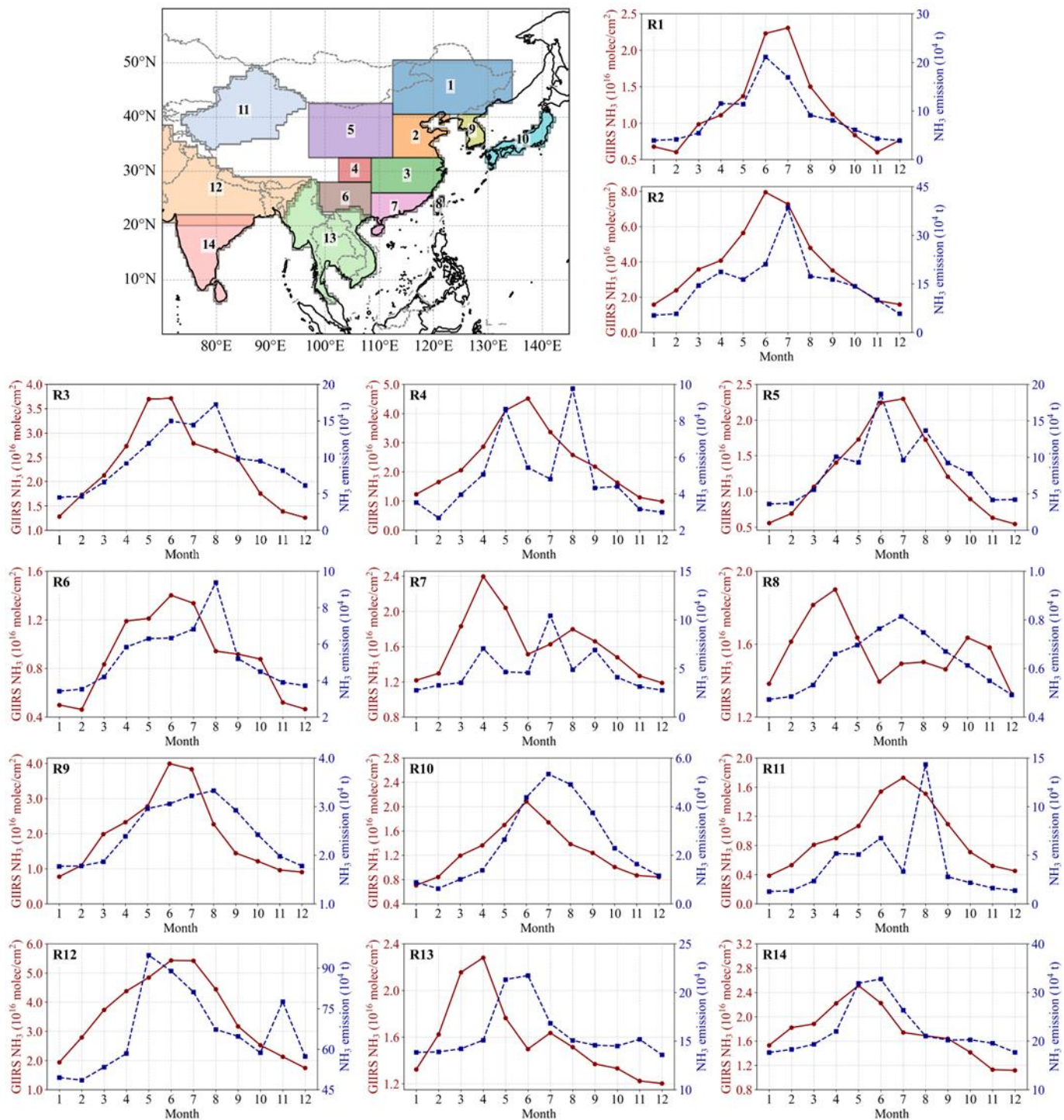
321 Figure 5 illustrates the months corresponding to the maximum NH₃ concentrations derived from GIIRS and IASI on a
 322 0.5° grid, while the result from CrIS, which is highly scattered at this scale, is shown on a 1° grid in Fig. S6. The spatial pattern
 323 shows a clear north-south gradient in the timing of NH₃ peaks. In the northern regions of East Asia, NH₃ columns generally

324 peak in June and July, which could be attributed to enhanced volatilization from agricultural soils, livestock operations, and
325 other sources (e.g., composting facilities and wastewater treatment plants) under high-temperature conditions (Li et al., 2024).
326 Irrigated croplands in the North and Northeast China Plains also exhibit a secondary spring maximum (Fig. S7) associated
327 with extensive fertilizer use and animal feeding operations. In contrast, the regions of southern China, India, and Southeast
328 Asia, characterized by a tropical monsoon climate, exhibit earlier NH_3 peaks, generally occurring from March to May. The
329 peak period coincides with their first cropping season, which involves intensive nitrogen fertilizer application. The warm and
330 humid conditions in these regions further promote NH_3 volatilization from soils and livestock waste. Following the onset of
331 the rainy season in June-July, atmospheric NH_3 concentrations decline sharply (such as R7, R8, R13, R14 in Fig. 6), primarily
332 due to enhanced wet scavenging processes. This seasonal pattern aligns with findings from multiple studies reporting a distinct
333 “late dry season-early wet season” NH_3 maximum in tropical regions (e.g., Chen et al., 2020; Liu et al., 2019). Spring is a
334 period of intense fire activity in the Indochina Peninsula, which is largely driven by residue burning, land-clearing, and
335 naturally flammable vegetation during the dry season (Chang et al., 2021; Vadrevu et al., 2019). The NH_3 maxima mainly
336 occur in March-April, and the consistent spatial distribution of these NH_3 peaks observed by GIIRS and IASI over Southeast
337 Asia suggests the influence of biomass burning associated with fires on its seasonal variations. In addition, bimodal local
338 maxima, with peaks of comparable magnitude, are also observed in regions such as central India (from May to September),
339 Guangdong in southern China (typically in April and August), and the transboundary region between the Mekong Delta in
340 Vietnam and Yunnan in China (March-April and June-July).

341 In general, the spatial and temporal distributions of NH_3 peaks largely agree with the previous studies of Van Damme et
342 al. (2015) and Shephard et al. (2020). Minor discrepancies between GIIRS and IASI result from differences in observational
343 accuracy and retrieval algorithms, as discussed above. Satellite-observed NH_3 seasonal cycles are driven by the interplay of
344 agricultural activities and climatic conditions, leading to deviations from seasonal patterns of anthropogenic emissions (Fig.
345 S8). Several studies have reported that NH_3 emissions inferred from satellite observations exhibit distinct seasonal variations
346 that can differ from those of the NH_3 columns (Li et al., 2026; Kumar et al., 2025). Therefore, we focus on the spatial
347 distribution of NH_3 enhancements, relative to regional background levels, as captured by different satellites.



348
 349 **Figure 5. The months with NH₃ column peaks observed by FY-4B/GIIRS from July 2022 to June 2025 and IASI from January 2022**
 350 **to June 2025 on a 0.5° × 0.5° grid. GIIRS results for the full daytime period (07:00–19:00 LST) are presented here for clarity, as**
 351 **morning and afternoon observations show consistent seasonal patterns (not shown).**



352
353
354

Figure 6. Monthly variations of GHIRS-derived NH₃ columns from July 2022 to June 2025 and NH₃ total emissions from the MIX inventory in 2017. Colored boxes specify spatial domains of 14 subregions (Sect. 2.5.2).

355 After removing monthly backgrounds derived from predefined regions (Fig. S9), NH₃ enhancements (Fig. 7) reveal a
356 spatial pattern of anthropogenic emissions that is highly consistent with the MIX emission inventory (Fig. 1). Apart from the
357 major agricultural emission regions mentioned above, some regions (e.g. Hyderabad and Vijayawada in India) also show
358 elevated NH₃ levels compared to the background during autumn and winter, likely influenced by dense urban and industrial
359 activities. Due to data discrepancies in local overpass times and sensor sensitivities among the polar-orbiting and geostationary
360 satellites (Shephard et al., 2025), the enhancement values detected by CrIS are 0.50 ± 0.64 and $0.74 \pm 0.90 \times 10^{16}$ molec/cm²
361 lower than those detected by GIIRS and IASI, respectively. These inter-satellite differences can lead to inconsistencies in the
362 observed NH₃ enhancements across various source regions, particularly over the Sichuan Basin, the Ningxia Irrigation Plain,
363 and the urban and biomass-burning regions of Southeast Asia. Compared with IASI and CrIS observations at different local
364 times, GIIRS provides consistent and reliable measurements throughout the daytime, enabling accurate characterization of
365 spatial and temporal variations in NH₃ concentrations across distinct emission source regions.

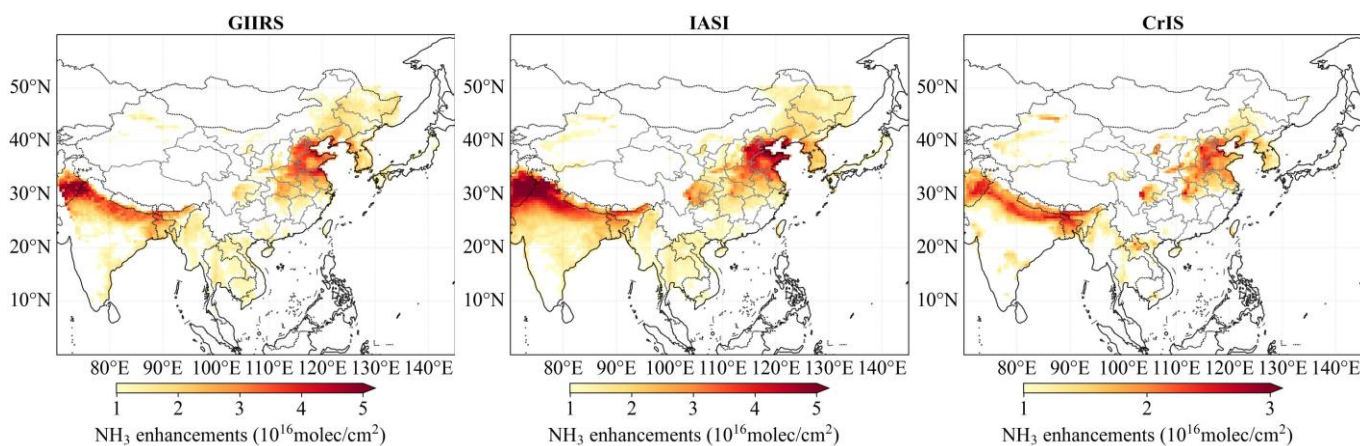


Figure 7. Spatial distribution of NH₃ enhancements derived from satellite observations (GIIRS, IASI, and CrIS). Note that the color bar for CrIS differs from those for GIIRS and IASI, and abnormal NH₃ enhancements over the Tibetan Plateau have been excluded.

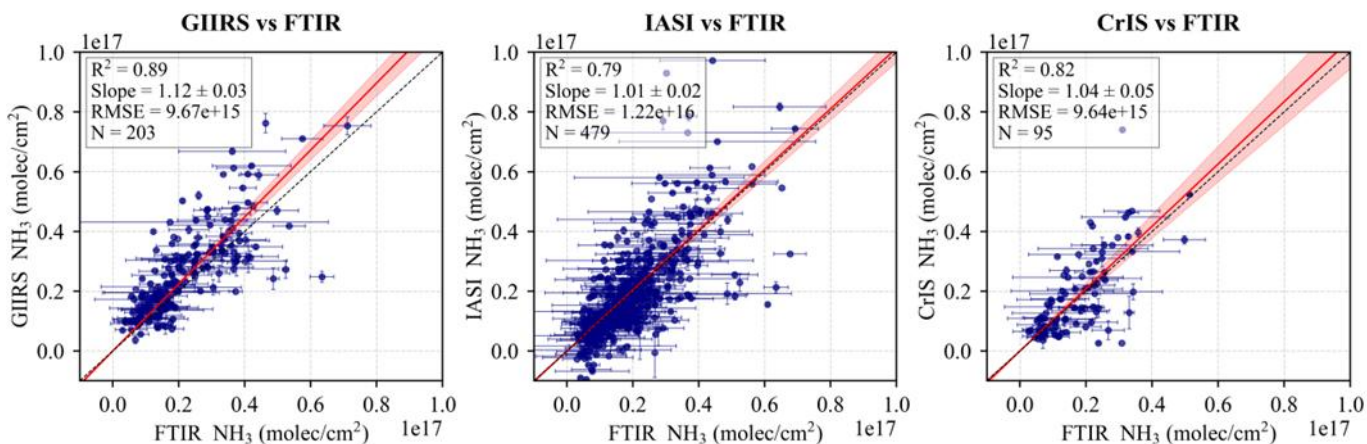
369 3.2 Inter-comparison of NH₃ variations at the Hefei station

370 To evaluate the data accuracy of GIIRS-derived NH₃ columns and assess the consistency of temporal variations with
371 polar-orbiting satellite measurements, we compared the satellite-based observations with ground-based FTIR measurements
372 at the Hefei station. Satellite data within a 0.25° latitude/longitude radius around the Hefei station (Fig. S10) were selected and
373 averaged on an hourly scale. A linear regression through the origin was applied to evaluate the proportional agreement between
374 the datasets.

375 Figure 8 shows scatter plots comparing NH₃ columns retrieved from satellite observations and FTIR measurements during
376 their overlapping periods. Overall, the satellite-derived NH₃ columns show good agreement with the FTIR data, with Pearson
377 correlation coefficients (R) exceeding 0.70, although satellite values are generally slightly higher. Among the satellites, GIIRS
378 agrees best with FTIR in terms of the highest correlation and the low root mean square error (RMSE). However, GIIRS exhibits
379 a relative systematic bias toward overestimating NH₃ columns, as indicated by its regression slope (1.12) being notably larger

380 than those of IASI and CrIS. When measurement uncertainties were taken into account, regression analysis using the
381 orthogonal distance regression (ODR) method yielded an increased slope of 1.24 (Fig. S11), indicating that GIIRS tends to
382 produce systematically higher NH₃ columns than IASI and CrIS.

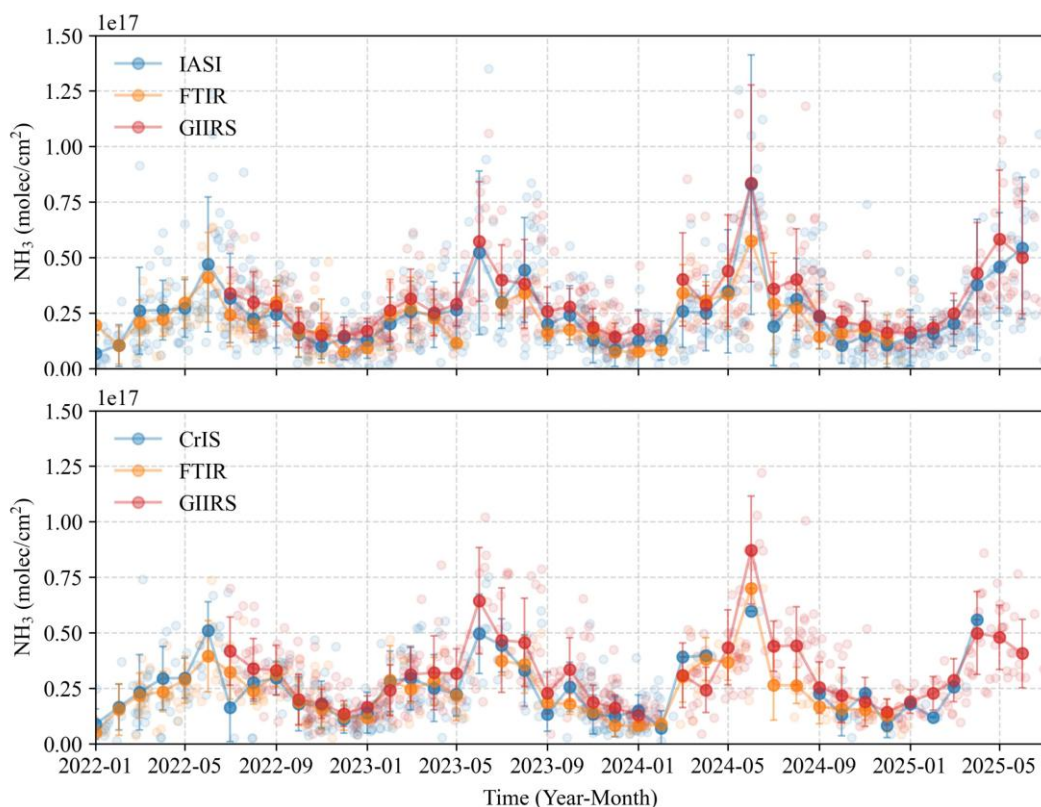
383 Although the overestimation of GIIRS becomes more pronounced in afternoon observations (Fig. S12), the corresponding
384 data conversely show improved consistency, which is characterized by higher R² and lower RMSE values. This is related to
385 the fact that the inversion accuracy of GIIRS observations is affected by TC and boundary layer conditions. High NH₃ columns
386 and significant TC represent favorable conditions for retrieving NH₃ from satellite observations (Zeng et al., 2023a; Clarisse
387 et al., 2010). As illustrated in Fig. S13, large positive TC between 11:00 and 15:00 LST enhances measurement sensitivity,
388 leading to lower retrieval errors. GIIRS NH₃ column retrievals are most reliable when TC exceeds 5 K, a condition
389 predominantly observed during summer daytime hours (7:00–19:00 LST).



390
391 **Figure 8. Cross-validation of hourly NH₃ columns from GIIRS, IASI, and CrIS with FTIR measurements at the Hefei station. The**
392 **overlapping periods span January 2017 (IASI), March 2019 (CrIS), and July 2022 (GIIRS) to December 2024. GIIRS data**
393 **encompass all daytime hours, while IASI and CrIS data correspond specifically to their respective overpass times.**

394 The Hefei station and its surrounding regions predominantly practice a rice-wheat rotation, with rice and winter wheat
395 typically sown in spring (around May) and autumn (around October), respectively. According to the MIX emission inventory,
396 agricultural ammonia emissions in this region exhibit two primary peaks in June and August, which are associated with local
397 agricultural practices including livestock waste management, nitrogen fertilizer application, and irrigation activities during the
398 rice growing season (Hou et al., 2020). Smaller peaks occur in October-November and April, corresponding to the rice
399 harvest/wheat sowing period and the wheat regreening fertilization stage, respectively. Driven jointly by agricultural emission
400 intensity and meteorological conditions such as high temperatures, the atmospheric NH₃ concentrations observed by satellites
401 and ground-based FTIR show consistent seasonal cycles, peaking in summer (June-August) and reaching a minimum in winter
402 (November-January). Figure 9 shows the monthly NH₃ time series observed by satellites and FTIR at different local overpass
403 times. GIIRS and IASI show closely matched NH₃ peaks in June. The systematic overestimation of peak values by GIIRS
404 relative to CrIS and FTIR is consistent with an inherent data bias as shown in Fig. 8.

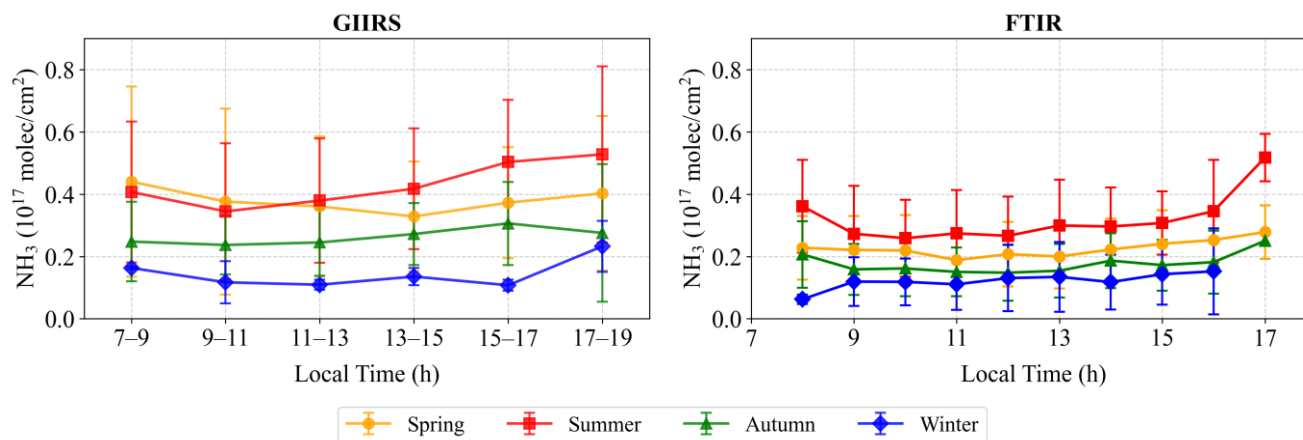
405 Notably, GIIRS-derived NH_3 columns in June 2024 were significantly higher than those in the same month of 2023 and
406 2025, with increases of 1.46 and 1.67 times during morning overpass time (~9:30 LST), and 1.35 and 2.15 times during
407 afternoon overpass time (~13:30 LST), respectively. Such pronounced variability is likely linked to extreme weather events
408 reported in the region, such as persistent heatwaves and abrupt drought-flood transitions (Zhou et al., 2025; Ding et al., 2024).
409 Morning observations from IASI align with GIIRS data, showing that NH_3 concentrations in June 2024 reached 1.43 to 2.62
410 times the levels recorded in the years 2017–2025 (specifically, 1.59 and 1.53 times those of 2023 and 2025, respectively).
411 Similar interannual changes were observed by CrIS and FTIR in June 2024, with NH_3 levels increasing by factors of 1.17–
412 1.53 and 1.40–2.28 compared with previous years, respectively, despite a data gap in June 2023 for FTIR.



413
414 **Figure 9. Time series of monthly NH_3 columns at the Hefei station from satellite-based and ground-based observations,**
415 **corresponding to different local overpass times of polar-orbiting satellites for morning (~9:30 LST) and afternoon (~13:30 LST).**
416 **The light-colored, semi-transparent points represent daily mean values at different local times.**

417 When comparing GIIRS-based NH_3 columns at different local times, afternoon concentrations are generally higher than
418 those in the morning, with the largest differences observed in summer (July–August) and the smallest in autumn and winter.
419 To more accurately characterize daytime NH_3 variations, we further applied strict data filtering criteria by retaining only
420 retrievals with $\text{TC} > 5 \text{ K}$ to ensure high sensitivity to near-surface NH_3 . Over the three-year period, 37 high-quality observation
421 days were identified, each providing six consecutive two-hour interval observations from 07:00 to 19:00 LST (Fig. S14). The

422 maximum diurnal amplitude occurs in summer, reaching over 1.5×10^{16} molec/cm². Except for autumn, all three other seasons
 423 exhibit relatively high NH₃ concentrations around 7:00 and 17:00 LST, a pattern that aligns well with the diurnal variations
 424 reported by Wang et al. (2022) based on FTIR measurements (Fig. 10). However, NH₃ retrievals from FTIR lack sufficient
 425 valid observations within a single day, making it difficult to consistently capture the intra-day variability in NH₃ across different
 426 dates.



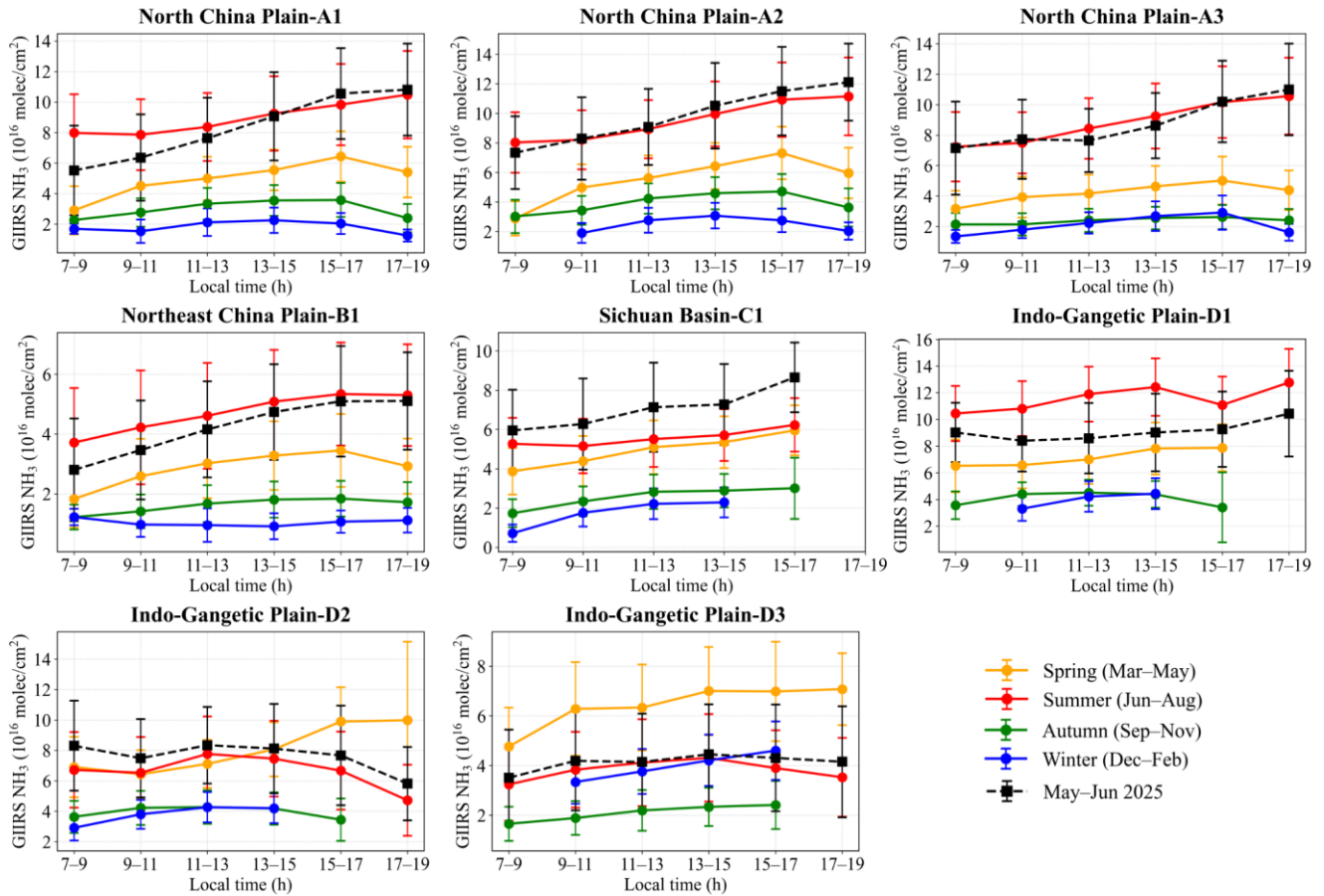
427
 428 **Figure 10. Daytime NH₃ variations observed by GIIRS and FTIR in different seasons. The seasonal mean NH₃ from GIIRS are**
 429 **calculated based on 37 high-quality days in Fig. S14.**

430 Moreover, the FTIR station is situated in a transitional zone between urban and suburban areas. A spatial domain with a
 431 radius of 0.25° used in this study encompasses GIIRS sampling points from both urban and agricultural regions (Fig. S10). To
 432 assess spatial variability of NH₃, GIIRS retrievals with TC > 5 K within this spatial domain were classified into urban and non-
 433 urban categories, and their daytime variations were statistically analyzed across seasons over three years. As shown in Fig.
 434 S15, NH₃ concentrations in non-urban areas are consistently and significantly higher than those in urban areas during spring
 435 and summer, indicating the strong contribution of agricultural activities to ambient NH₃ levels. Particularly in spring,
 436 statistically significant differences are most pronounced during 7:00–9:00 and 17:00–19:00 LST, corresponding to time
 437 windows of fertilizer application and livestock activity. During winter, higher NH₃ levels in the morning and late afternoon are
 438 mainly observed in urban areas, likely reflecting the impact of traffic emissions. These findings highlight the importance of
 439 high-frequency satellite observations for dynamic monitoring of NH₃ variations, and the contribution of agricultural activity
 440 in shaping the diurnal NH₃ variability.

441 3.3 Daytime NH₃ variations in major agricultural regions

442 We focused on eight major agricultural source areas located in the North China Plain and the Northeast China Plain, the
 443 Sichuan Basin, and the Indo-Gangetic Plain, to further investigate daytime variations in NH₃ columns. These areas are
 444 characterized by high NH₃ column concentrations and emissions, generally flat terrain, and a large proportion of irrigated
 445 cropland (as shown in Figs. S16–17). To ensure sufficient measurement sensitivity to near-surface NH₃, only GIIRS

446 observations with TC greater than 5 K were retained, thereby excluding cases with low information content. During autumn
 447 and winter, available observations are sparse in the early morning and late afternoon. Here, GIIRS-observed daytime variations
 448 of NH_3 columns across different seasons (Fig. 11) and the corresponding spatial distributions for each study region (Figs. 12–
 449 14, Figs. S18–20) are presented, with comparisons to anthropogenic NH_3 emissions (Fig. S17) and GEOS-CF model
 450 simulations (Figs. S21–24). Despite significant differences between model-simulated and satellite-based NH_3 columns, we
 451 focused on analyzing the daytime variations and their spatial distributions in representative months of May–June (NH_3 peak
 452 months) in 2025.
 453



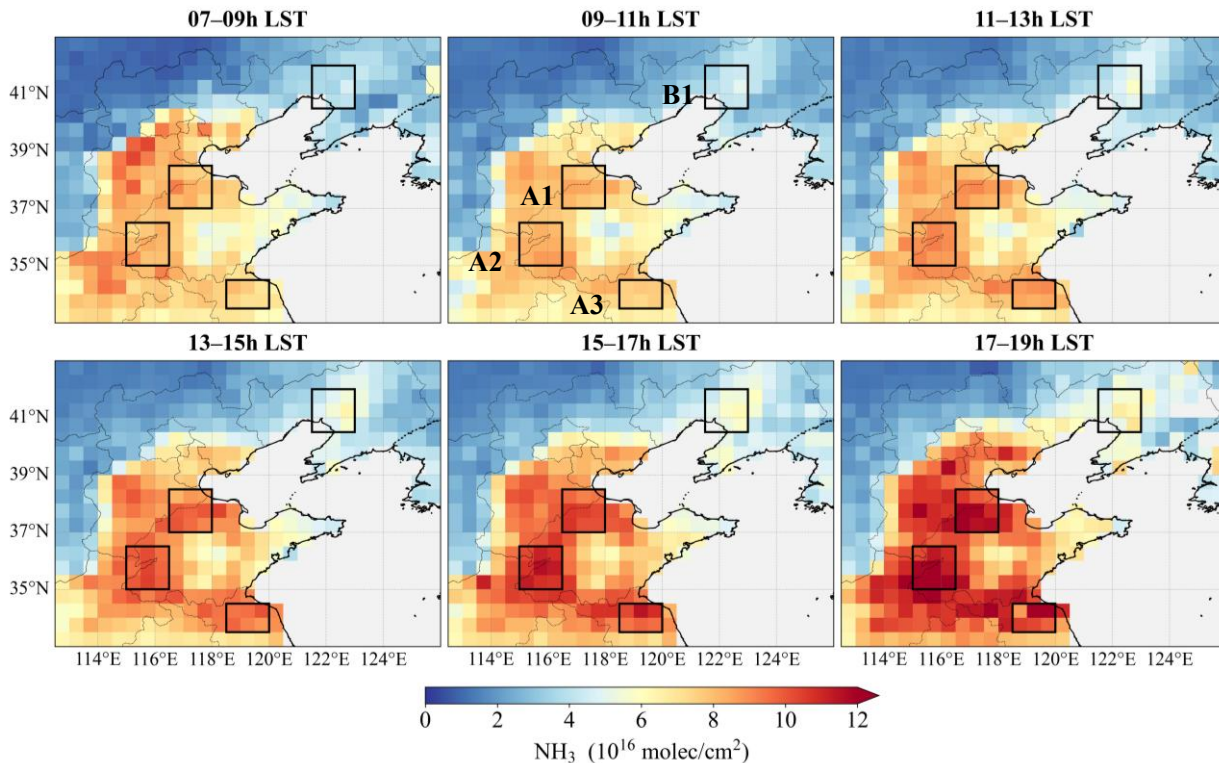
454
 455
 456 **Figure 11. Daytime NH_3 variations for major agricultural emission areas observed by GIIRS in different seasons.**

457
 458 The North China Plain is characterized by extensive irrigated croplands with winter wheat-maize rotation and widespread
 459 small-scale livestock farming concentrated in east-central provinces, including Henan, Shandong, and Hebei. Due to intensive
 460 agricultural and livestock activities, dense industrial emissions and heavy urban traffic, the region ranks among the most

461 polluted regions in China. The spatial distribution of local NH_3 high values across different seasons shows considerable
462 variations, especially during the late afternoon in the spring and summer, which may indicate a change in emission hotspots
463 (Fig. 12 and Fig. S18). Across the three selected areas (A1-A3), GIIRS observations reveal a consistent temporal pattern of
464 NH_3 columns, with values increasing from early morning to late afternoon in summer but generally declining after 15:00 LST
465 in other seasons. In summer, the mean variations in GIIRS NH_3 column amplitudes for the afternoon and morning are 22%,
466 27%, and 29%, respectively, while in May and June 2025, these variations increased to 56%, 38%, and 32%, respectively.

467 The Northeast China Plain is a key grain production region, particularly for maize, soybeans, and rice. Agriculture is
468 highly mechanized, and livestock farming is carried out on a large scale. Because agricultural emission sources are spatially
469 concentrated and geographically stable, the spatial pattern of NH_3 enhancements shows little variation at different local times
470 (Fig. 12). The B1 area is located in the estuarine delta, with large cities such as Shenyang and Anshan to the east. Due to low
471 population density and limited industrial activity, NH_3 emissions in this area are primarily associated with fertilizer application
472 and animal husbandry, resulting in relatively lower levels than those in other areas. GIIRS observations show that NH_3 columns
473 are at markedly reduced levels, approximately 52% of those in the North China Plain, but follow a similar diurnal cycle, with
474 the variation amplitude in summer being comparable (25% for 3 years, 43% for May-June 2025). The difference is that in
475 winter, the diurnal variation also shows higher NH_3 columns in the morning (7:00–9:00 LST), which may be related to traffic
476 emissions and the effects of meteorological conditions (such as temperature and humidity changes) in the early morning.
477 Ground-based studies have reported that the peak atmospheric NH_3 concentration typically occurs in the morning, as observed
478 in the urban area of Beijing (Gu et al., 2022) and in the rural areas of Xianghe (He et al., 2020), Xinxiang (Teng et al., 2017),
479 Shanghai (Wang S. et al., 2015), and Hefei (Wang et al., 2022).

480

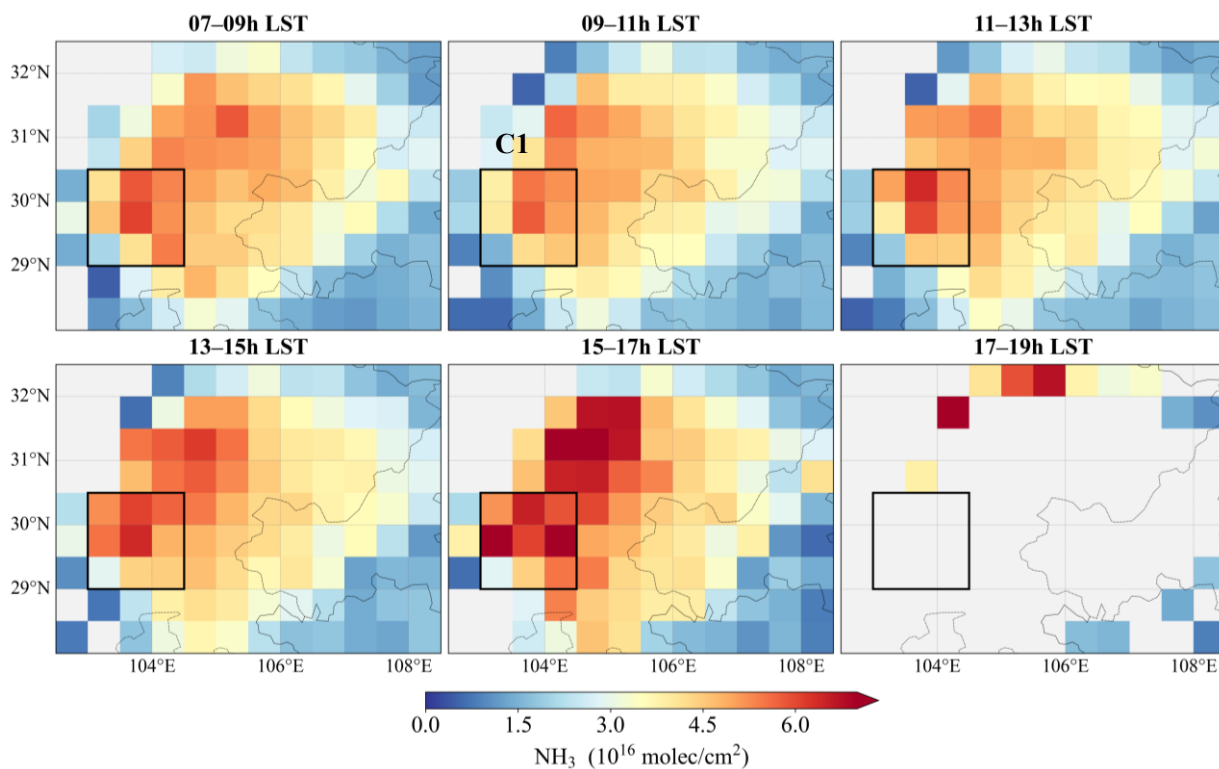


481
482 **Figure 12. Daytime NH₃ variations observed by GIIRS in summer from July 2022 to June 2025 in the North-Northeast China Plain.**

483 The Sichuan Basin, located in southwestern China, is an important agricultural region encompassing the Chengdu-
484 Chongqing urban agglomeration. Ammonia emissions exhibit a clear east-west gradient, reflecting regional differences in
485 agricultural practices and livestock management (Li et al., 2021; Zhang, L., et al., 2018; Kang et al., 2016). Studies based on
486 IASI observations indicate that NH₃ hotspots in the Sichuan Basin are primarily concentrated in the Chengdu Plain, the
487 southern urban clusters, and northwestern Sichuan, where agricultural sources dominate ammonia emissions (Yang et al., 2024;
488 Dammers et al., 2019; Van Damme et al., 2018). GIIRS observations show that NH₃ columns are significantly enhanced in the
489 western regions, particularly along the Mianyang-Deyang-Chengdu-Meishan-Leshan corridor (Fig. 7 and Fig. 13), which is
490 associated with intensive agricultural activity and urban-industrial emissions. The basin's unique topography and
491 meteorological conditions such as frequent temperature inversions result in very few valid NH₃ observations after 17:00 LST.
492 Across different seasons, NH₃ columns generally exhibit an increasing trend from morning to afternoon. In spring and summer,
493 seasonal mean NH₃ concentrations show relatively small differences because agricultural sources dominate and vertical mixing
494 is enhanced by changes in boundary layer height, with daytime NH₃ variations of 27% and 23%, respectively. The largest
495 daytime variation occurs in winter, when afternoon values are 1.46 times higher than those in the morning.

496

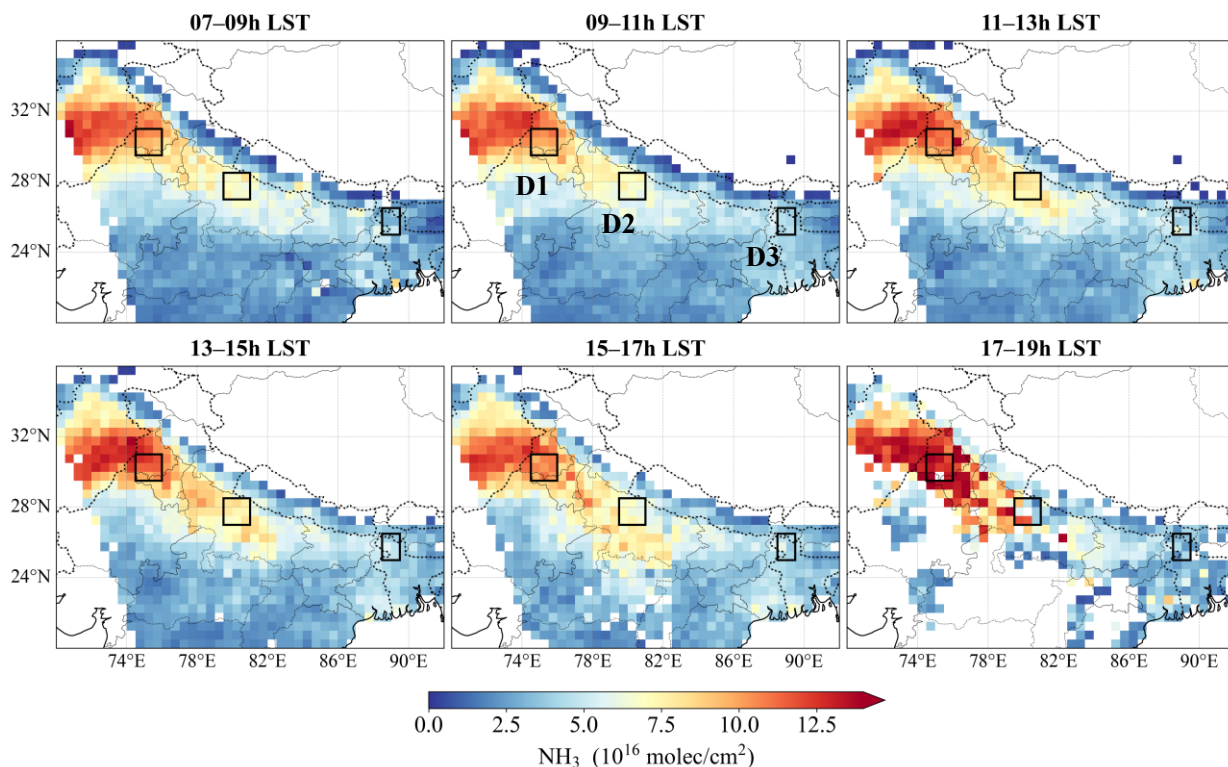
497



498
499 **Figure 13. Daytime NH₃ variations observed by GIIRS in summer from July 2022 to June 2025 in the Sichuan Basin.**

500 The Indo-Gangetic Plain, South Asia's most extensive alluvial plain, spans Pakistan, northern India, and Bangladesh. The
 501 region is densely populated and intensively farmed, producing rice, wheat, sugarcane, and vegetables, often under irrigated
 502 and mechanized conditions. Fertilizer application, livestock excretion, industrial activities, and high population density lead
 503 to significant NH₃ and reactive nitrogen emissions, reaching their maximum over the Punjab region in Pakistan. We selected
 504 three areas that are located in Punjab, Uttar Pradesh, and Bangladesh, respectively (Fig. 14). Differences in NH₃ emission
 505 sources and climatic conditions across these regions lead to pronounced seasonal variations in NH₃ concentrations. The
 506 daytime variation amplitudes of NH₃ columns are highest in spring, which are 17%, 32%, and 21% for D1, D2, and D3,
 507 respectively. However, under the coupled conditions of abundant precipitation and strong solar radiation in summer, NH₃
 508 columns in the D2 and D3 areas reach their peak around 13:00 LST.

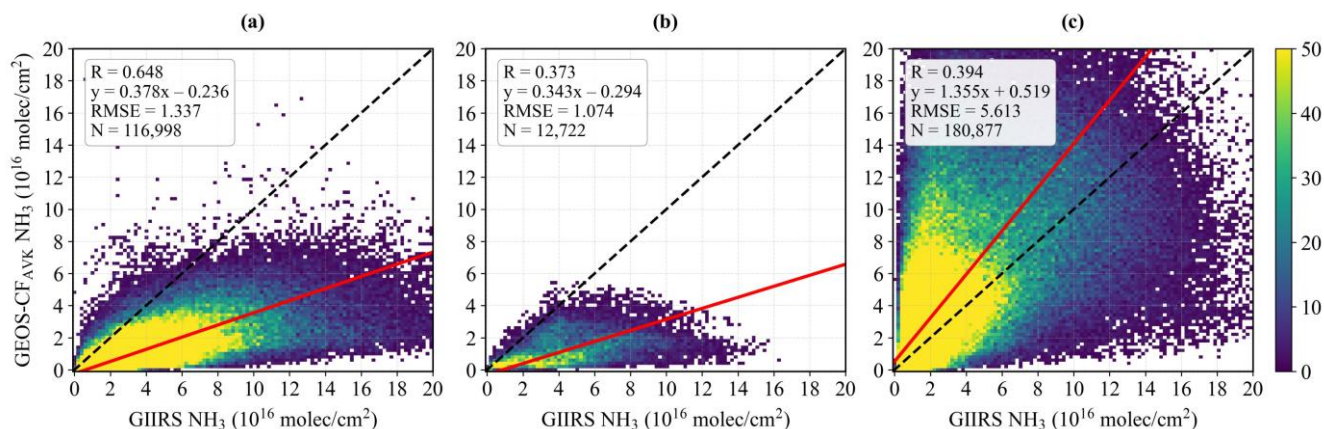
509
510



511
512 **Figure 14. Daytime NH₃ variations observed by GIRS in summer from July 2022 to June 2025 in the Indo-Gangetic Plain.**

513 The diurnal variation of atmospheric NH₃ column concentrations is primarily influenced by surface emissions, boundary
 514 layer dynamics, and gas-particle partitioning associated with meteorological conditions (Lan et al., 2024; Behera et al., 2013).
 515 In these main agricultural source areas, NH₃ concentrations generally rise from morning to afternoon, driven by diurnal
 516 variations in temperature and humidity that shift the gas-particle equilibrium toward the gaseous phase. The daytime NH₃
 517 variations simulated by the GEOS-CF model for May-June 2025 range from 7% to 36%, slightly lower than the variations
 518 observed by GIRS (10% to 56%). However, the GEOS-CF model was unable to accurately reproduce the spatial pattern of
 519 NH₃ enhancements in the Sichuan Basin, which can be largely attributed to the bottom-up emission inventory and the influence
 520 of complex topography and local climatic conditions. After considering the vertical sensitivities of satellite retrievals, the AVK-
 521 smoothed model data resulted in an overall reduction of $12 \pm 38\%$ in the model NH₃ columns over the Sichuan Basin. However,
 522 considerable discrepancies in the spatial distribution remain relative to the satellite observations. Figure 15 presents a cross-
 523 comparison between the satellite-derived NH₃ columns and the AVK-smoothed model data in May-June 2025. Over the North-
 524 Northeast China Plain, the model underestimates NH₃ columns by 62% on average, with a standard deviation of 45%, whereas
 525 over the Sichuan Basin, the underestimation reaches 65%, with a standard deviation of 30%. In contrast, the model generally
 526 overestimates NH₃ columns over the Indo-Gangetic Plain. Regarding the spatial and temporal patterns of diurnal variations

527 (Figs. S25–28), the largest discrepancies are observed in the areas of C1 in the Sichuan Basin and D1 in the Indo-Gangetic
528 Plain, suggesting that the model has limited capability to simulate NH₃ in these areas and may require improvements through
529 satellite-observed constraints to improve simulation accuracy.



530
531 **Figure 15. Comparison of NH₃ columns in May and June 2025 from GIIRS observations and GEOS-CF AVK-smoothed model**
532 **simulations for (a) the North China Plain and the Northeast China Plain, (b) the Sichuan Basin, and (c) the Indo-Gangetic Plain.**
533 **The model data is calculated by applying the AVKs from satellite retrievals to NH₃ profile (see Text S1).**

534 4 Conclusions and Perspectives

535 The geostationary satellite observations from FY-4B/GIIRS provide a unique opportunity to monitor the diurnal variations
536 of atmospheric NH₃ over East Asia, yet current research on this topic remains limited. In this study, we present a comprehensive
537 analysis of three years of FY-4B/GIIRS observations from July 2022 to June 2025, revealing the spatiotemporal variations of
538 NH₃ across East Asia and the distinctive daytime variations in agricultural emission regions.

539 NH₃ column concentrations from GIIRS observations exhibit pronounced local enhancements over major emission
540 regions, particularly in flat agricultural plains (e.g. the North China Plain, the Northeast China Plain, the Indo-Gangetic Plain,
541 the Ningxia Irrigation Plain, the Wei River Plain, the Jiangnan Plain, the Mekong Delta in Vietnam, the Chao Phraya River
542 Plain in Thailand) with intensive crop cultivation and animal husbandry, as well as smaller-scale accumulation in
543 topographically confined areas such as valleys and basins (e.g. the Sichuan Basin, oasis agriculture in the arid regions of
544 Xinjiang in China, the Fergana Valley in Uzbekistan). After removing background levels derived from predefined reference
545 regions, NH₃ enhancements show a consistent spatial pattern with anthropogenic emissions from the bottom-up MIX Asia
546 emission inventory, and highlight these major emission source regions. The spatial distribution of NH₃ derived from GIIRS
547 agrees well with polar-orbiting satellite observations from IASI and CrIS.

548 The timing of peak NH₃ in the seasonal cycle primarily reflects agricultural activities related to fertilizer application and
549 is modulated by climatic factors such as temperature. For example, NH₃ columns generally exhibit a summer maximum (June-
550 July) and a secondary spring maximum (April) in the North China Plain and Northeast China Plain. In southern regions of
551 China, India, and Southeast Asia, NH₃ peaks during the late dry season (March-May) and declines sharply in the early wet

552 season (June-July). Overall, regional differences in the timing of peak months follow a north-south gradient. Comparison with
553 ground-based FTIR measurements and satellite-based IASI and CrIS observations show generally good agreement, yielding a
554 correlation coefficient of 0.77 and an RMSE of 9.67×10^{15} molec/cm² relative to FTIR, while also consistently capturing the
555 temporal variability of NH₃ columns.

556 This study reports the detailed daytime variations of NH₃ columns observed by FY-4B/GIIRS over the North China Plain,
557 the Northeast China Plain, the Sichuan Basin, Hefei, and the Indo-Gangetic Plain. The NH₃ columns during the day generally
558 increase from early morning to late afternoon, showing similar temporal variations to those observed by ground-based FTIR
559 measurements at Hefei and simulated by GEOS-CF model in the main agricultural source areas. Crucially, GIIRS provides
560 substantial advantages by accurately characterizing spatial distributions and enabling continuous daily observations. GIIRS in
561 the infrared is complementary to the Geostationary Environment Monitoring Spectrometer (GEMS; Kim et al., 2020), which
562 operates in the ultraviolet/visible (UV/VIS) spectral range and provides hourly observations of trace gases such as NO₂ and
563 SO₂ over East Asia. The synergy between GIIRS and GEMS enables joint investigations of NH₃ and NO₂, offering new
564 opportunities to better quantify reactive nitrogen budgets and assess their impacts on air quality and climate. The upgraded
565 FY-4C/GIIRS was launched in December 2025, further enhancing the FY-4 geostationary observational capabilities. Compared
566 to its predecessor FY-4B/GIIRS, which provides a spatial resolution of 12 km and a temporal resolution of 2 hours, FY-
567 4C/GIIRS achieves a significant improvement to 8 km and 1 hour, respectively. This emerging satellite constellation will offer
568 unprecedented opportunities for seamless hourly coverage to monitor diurnal cycles and emission processes across East and
569 South Asia, thereby improving our understanding of atmospheric chemistry and supporting the development of more effective
570 air pollution mitigation strategies.

571

572 Appendix: The interpretation and calculation of column AVK

573 In the profile-scaling optimal estimation framework, the column AVK (unitless) represents the change in the retrieved
574 total NH₃ column (molec/cm²) with respect to a perturbation of the partial NH₃ column (molec/cm²) at a given atmospheric
575 layer. For example, if the true NH₃ partial column in the first layer near the surface increases by 1.0×10^{16} molec/cm², whereas
576 the retrieval algorithm only detects an increase of 0.4×10^{16} molec/cm² in the final retrieved total column, the resulting column
577 AVK for the first layer is 0.4. A value of 1.0 would imply perfect sensitivity to that layer. As a hyperspectral sounder has
578 varying sensitivities to different altitudes and the spectral signatures of NH₃ molecules vary at different altitudes, the retrieved
579 total column is not uniformly sensitive to NH₃ molecules at all heights. The one-dimensional column AVK thus provides a
580 crucial diagnostic metric to understand where the retrieved column information is originating. This definition of column AVK
581 is conceptually similar to that from TCCON (Wunch et al., 2011) and IASI (Clarisse et al., 2023). By contrast, the conventional
582 matrix AVK from optimal estimation quantifies how much information is retrieved from the measurement (Shephard et al.,
583 2011, 2015), and the sum of each row of AVK provides an estimate of the fraction of retrieval information contributed by the
584 measurement rather than the a priori at the corresponding altitude. When the information content of the measurement is high
585 or the retrieval loosely constrained, the AVK values approach the unit matrix. Conversely, when the information content is low
586 or the retrieval is heavily constrained, the AVK values tend toward zero and the solution remain close to the a priori. A detailed
587 discussion on the difference between column AVK and matrix AVK can be referred to Clarisse et al. (2023).

588 The column AVK is calculated following the formalism of the full matrix AVK from optimal estimation, which is
589 expressed as:

$$590 \text{ Column AVK} = G K_{GasProf} \quad (A1)$$

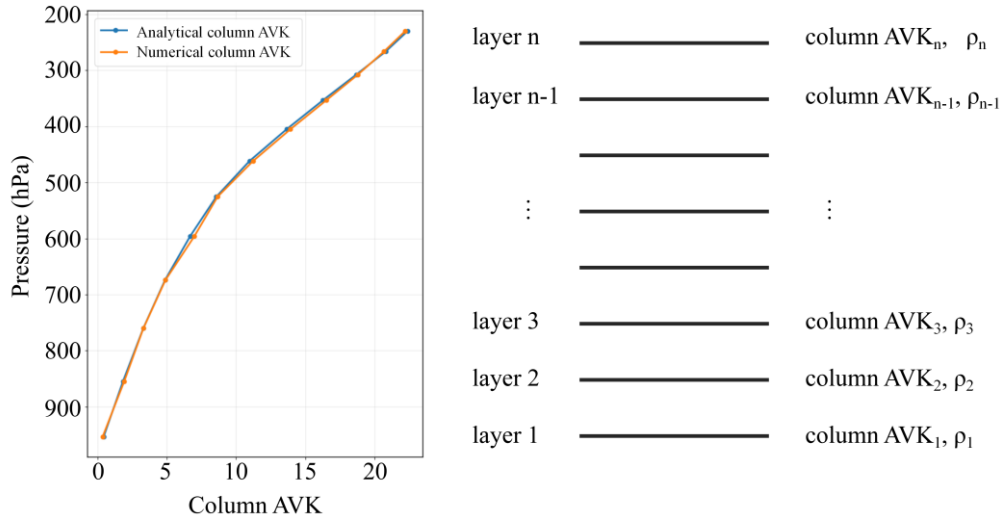
591 where $K_{GasProf}$ is the layer-resolved NH₃ Jacobian quantifying the sensitivity of radiance to layer-specific NH₃ partial column
592 perturbations. $K_{GasProf}$ is calculated using the radiative transfer model for each retrieval. The gain matrix G is given by:

$$593 G = (K_{col}^T S_{\epsilon}^{-1} K_{col} + S_a^{-1})^{-1} K_{col}^T S_{\epsilon}^{-1} \quad (A2)$$

594 where K_{col} is the total-column NH₃ Jacobian quantifying the sensitivity of radiance to total NH₃ column, S_{ϵ} and S_a are the
595 noise covariance matrix for the measured radiances and the a priori covariance matrix for the retrieval.

596 To verify the analytical column AVK calculated from Eq. (A1), observation simulation experiments were conducted to
597 calculate the corresponding numerical column AVK for comparison. An observation over the North China Plain (41.97°N,
598 122.50°E) on 15 July 2025 was selected, with a surface pressure of 1002.65 hPa, surface temperature of 302.49 K, and lowest-
599 layer air temperature of 297.46 K. The “true” NH₃ profile was generated by scaling the a priori profile from Zeng et al. (2023a)
600 by a factor of 10 (approximate total column: 9.49×10^{16} molec/cm²), which was also used as the a priori profile for all retrievals.
601 We first simulated the “true” radiance spectrum from the “true” profile, added Gaussian random noise, and ran the retrieval
602 algorithm 100 times to obtain the mean retrieved total column, which is close to the true total column. The analytical column
603 AVK solution from this observation was then derived using Eqs. (A1) and (A2). Subsequently, we performed a layer-wise
604 perturbation test to derive the numerical column AVK. A fixed NH₃ perturbation of 1×10^{16} molec/cm² was individually added

605 to each of the 12 retrieval layers of the “true” profile, while keeping all other layers unchanged. For each perturbed layer, the
 606 noise-added retrieval was repeated 100 times to obtain the mean retrieved total column. The numerical column AVK was then
 607 calculated as the ratio of the retrieved total column change to the imposed “true” column increment (1×10^{16} molec/cm²). Figure
 608 A1 compares the analytical and numerical AVKs, showing good agreement between the two sets, thereby justifying the
 609 calculation of column AVK using Eqs. (A1) and (A2).



610
 611 **Figure A1. Comparison of the analytical and numerical column AVKs for a case over the North China Plain on 15 July 2024 (left**
 612 **panel). Schematic of the retrieval vertical layers from the surface to 200 hPa (right panel), consisting of n pressure levels (typically**
 613 **n = 11 or 12), with the layer-dependent column AVK values (column AVK_i) and the air density (ρ_i) of NH₃ at each layer.**

614 **Data availability.**

615 The GIIRS NH₃ data (July 2022 to June 2025) used in this study is publicly available on Zenodo (Zeng et al.,
616 2025; <https://doi.org/10.5281/zenodo.17193848>). Further updates on the data will be provided on the project website
617 (<https://fengyunair.github.io/>). The IASI L2 ammonia satellite observations are available from the AERIS data infrastructure
618 (<https://iasi.aeris-data.fr/>, last access: 16 September 2025). The CrIS Fast Physical Retrieval (CFPR) ammonia dataset is
619 created by the Environment and Climate Change Canada is publicly available
620 (https://hpfx.collab.science.gc.ca/~mas001/satellite_ext/cris/). The Hefei FTIR data are retrieved by Key Laboratory of
621 Environmental Optics and Technology, Anhui Institute of Optics and Fine Mechanics, Chinese Academy of Sciences (Wang
622 et al., 2022). The MIX emission inventory can be requested from the MEIC team (http://meicmodel.org.cn/?page_id=2721).
623 The GEOS-CF model data are available from High Performance Computing for Science, NASA Center for Climate Simulation
624 (<https://portal.nccs.nasa.gov/datashare/gmao/geos-cf/v1/das/Y2025/>, last access: 10 August 2025).

625 **Author contributions.**

626 MS and ZZ designed the study. MS carried out the result analysis and prepared the manuscript. ZZ and JH developed the
627 GIIRS NH₃ retrieval algorithm. MS, RZ, SH, and SL collected and analyzed the emission sets. WW provided the FTIR data.
628 RD, LZ, HC, ZC, and YG provided guidance on interpreting the satellite data and model simulations. ML provided guidance
629 on analyzing emission inventory. NG, LC, MVD, and CC provided the IASI data and guided the interpretation. MWS provided
630 the CrIS data and guidance. LL, CQ, FL, and CH provided guidance on analyzing GIIRS spectra. All authors reviewed and
631 proofread the paper. LC is a senior research associate supported by the Belgian F.R.S.-FNRS.

632 **Competing interests.** The contact author has declared that none of the authors has any competing interests.

633 **Disclaimer.** Publisher's note: Copernicus Publications remains neutral with regard to jurisdictional claims made
634 in the text, published maps, institutional affiliations, or any other geographical representation in this paper. While
635 Copernicus Publications makes every effort to include appropriate place names, the final responsibility lies with
636 the authors.

637 **Acknowledgements.** We acknowledge FY-4B/GIIRS L1 spectral data provided by the National Satellite
638 Meteorological Center (NSMC) of the China Meteorological Administration (CMA). We are grateful to the AERIS
639 data infrastructure for providing access to the IASI NH₃ data. We thank the ECCC for making the CrIS NH₃ data

640 publicly available. We also acknowledge the MEIC team for sharing the NH₃ emission dataset from MIX inventory
641 and the NASA Center for Climate Simulation(NCCS) for sharing NH₃ data from GEOS-CF model simulations,
642 and the ECMWF for sharing ERA-5 reanalysis data. This study was supported by the High-Performance Computing
643 Platform of Peking University.

644 **Financial support.** This study was supported by the National Natural Science Foundation of China (No. 42275142),
645 the China Postdoctoral Foundation (No. 2025M770242) and the National Key R&D Program of China (No.
646 2026YFE0102400, 2022YFA1003800).

647

648 References

- 649 Beer, R., Shephard, M. W., Kulawik, S. S., Clough, S. A., Eldering, A., Bowman, K. W., Sander, S. P., Fisher, B. M., Payne,
650 V. H., Luo, M., Osterman, G. B., and Worden, J. R.: First satellite observations of lower tropospheric ammonia and
651 methanol, *Geophys. Res. Lett.*, 35, L09801, <https://doi.org/10.1029/2008GL033642>, 2008.
- 652 Behera, S. N., Sharma, M., Aneja, V. P., and Balasubramanian, R.: Ammonia in the atmosphere: a review on emission sources,
653 atmospheric chemistry and deposition on terrestrial bodies, *Environ. Sci. Pollut. Res.*, 20, 8092–8131,
654 <https://doi.org/10.1007/s11356-013-2051-9>, 2013.
- 655 Bobbink, R., Hicks, K., Galloway, J., Spranger, T., Alkemade, R., Ashmore, M., Bustamante, M., Cinderby, S., Davidson, E.,
656 Dentener, F., Emmett, B., Erismann, J.-W., Fenn, M., Gilliam, F., Nordin, A., Pardo, L., and De Vries, W.: Global
657 assessment of nitrogen deposition effects on terrestrial plant diversity: A synthesis, *Ecol. Appl.*, 20, 30–59,
658 <https://doi.org/10.1890/08-1140.1>, 2010.
- 659 Bowman, K. W.: TROPESS CrIS-JPSS1 L2 Ammonia for Forward Stream, Summary Product V1, Goddard Earth Sciences
660 Data and Information Services Center (GES DISC), Greenbelt, MD, USA, available at:
661 <https://doi.org/10.5067/2Q7XUY6OTKY1> (last access: 18 July 2025), 2022.
- 662 Cady-Pereira, K. E., Guo, X., Wang, R., Leytem, A., Calkins, C., Berry, E., Sun, K., Müller, M., Wisthaler, A., Payne, V. H.,
663 Shephard, M. W., Zondlo, M. A., and Kantchev, V. H.: Validation of NH₃ observations from AIRS and CrIS against
664 aircraft measurements from DISCOVER-AQ and a surface network in the Magic Valley, *Atmos. Meas. Tech.*, 17, 15–
665 36, <https://doi.org/10.5194/amt-17-15-2024>, 2024.
- 666 Cady-Pereira, K., Payne, V., Bowman, K., Worden, J., Luo, M., Calkins, C., Kulawik, S., Whitten, K., and Fahy, K.:
667 TROPESS-AIRS-CrIS NH₃ Level 2 Product User Guide, Version 2.0, NASA Jet Propulsion Laboratory, Pasadena, CA,
668 available at: [https://docserv.gesdisc.eosdis.nasa.gov/public/project/TROPESS/User_Guides/TROPESS-AIRS-](https://docserv.gesdisc.eosdis.nasa.gov/public/project/TROPESS/User_Guides/TROPESS-AIRS-CrIS_NH3_L2_Product_User_Guide_2-22-21.pdf)
669 [CrIS_NH₃_L2_Product_User_Guide_2-22-21.pdf](https://docserv.gesdisc.eosdis.nasa.gov/public/project/TROPESS/User_Guides/TROPESS-AIRS-CrIS_NH3_L2_Product_User_Guide_2-22-21.pdf) (last access: 15 June 2024), 2021.
- 670 Cao, H., Henze, D. K., Shephard, M. W., Damers, E., Cady-Pereira, K. E., Alvarado, M., Lonsdale, C., Luo, G., Yu, F., Zhu,
671 L., Danielson, C. G., and Edgerton, E. S.: Inverse modeling of NH₃ sources using CrIS remote sensing measurements,
672 *Environ. Res. Lett.*, 15, 104082, <https://doi.org/10.1088/1748-9326/abb5cc>, 2020.
- 673 Cao, H., Henze, D. K., Zhu, L., Shephard, M. W., Cady-Pereira, K., Damers, E., and Capps, S. L.: 4D-Var inversion of
674 European NH₃ emissions using CrIS NH₃ measurements and GEOS-Chem adjoint with bi-directional and uni-directional
675 flux schemes, *J. Geophys. Res.-Atmos.*, 127, e2021JD035687, <https://doi.org/10.1029/2021JD035687>, 2022.
- 676 Chang, Y., Zou, Z., Zhang, Y., Deng, C., Hu, J., Shi, Z., Dore, A. J., and Collett, J. L. Jr.: Assessing contributions of agricultural
677 and nonagricultural emissions to atmospheric ammonia in a Chinese megacity, *Environ. Sci. Technol.*, 53, 1822–1833,
678 <https://doi.org/10.1021/acs.est.8b05984>, 2019.

679 Chang, Y., Zhang, Y.-L., Kawichai, S., Wang, Q., Van Damme, M., Clarisse, L., Prapamontol, T., and Lehmann, M. F.:
680 Convergent evidence for the pervasive but limited contribution of biomass burning to atmospheric ammonia in peninsular
681 Southeast Asia, *Atmos. Chem. Phys.*, 21, 7187–7198, <https://doi.org/10.5194/acp-21-7187-2021>, 2021.

682 Chen, F., Lao, Q., Li, Z., Chen, C., Zhou, X., and Zhang, S.: Monthly variations in the nitrogen isotope of ammonium in wet
683 deposition in a tropical city of South China, *Atmos. Chem. Phys.*, 20, 1062–1069,
684 <https://doi.org/10.4209/aaqr.2019.06.0303>, 2020.

685 Chen, J., Du, X., Liu, X., Xu, W., and Krol, M.: Estimation of ammonia emissions over China using IASI satellite-derived
686 surface observations, *Environ. Sci. Technol.*, 59, 9991–10000, <https://doi.org/10.1021/acs.est.4c10878>, 2025.

687 Chen, Y., Shen, H., Kaiser, J., Hu, Y., Capps, S. L., Zhao, S., Hakami, A., Shih, J.-S., Pavur, G. K., Turner, M. D., Henze, D.
688 K., Resler, J., Nenes, A., Napelenok, S. L., Bash, J. O., Fahey, K. M., Carmichael, G. R., Chai, T., Clarisse, L., Coheur,
689 P.-F., Van Damme, M., and Russell, A. G.: High-resolution hybrid inversion of IASI ammonia columns to constrain US
690 ammonia emissions using the CMAQ adjoint model, *Atmos. Chem. Phys.*, 21, 2067–2082, [https://doi.org/10.5194/acp-](https://doi.org/10.5194/acp-21-2067-2021)
691 [21-2067-2021](https://doi.org/10.5194/acp-21-2067-2021), 2021.

692 Chen, Z.-L., Song, W., Hu, C.-C., Liu, X.-J., Chen, G.-Y., Walters, W. W., Michalski, G., Liu, C.-Q., Fowler, D., and Liu, X.-
693 Y.: Significant contributions of combustion-related sources to ammonia emissions, *Nat. Commun.*, 13, 7710,
694 <https://doi.org/10.1038/s41467-022-35381-4>, 2022.

695 Choi, H., Park, M. E., and Bae, J.-H.: Distinct regional and seasonal patterns of atmospheric NH₃ observed from satellite over
696 East Asia, *Remote Sens.*, 17, 2587, <https://doi.org/10.3390/rs17152587>, 2025.

697 Clarisse, L., Clerbaux, C., Dentener, F., Hurtmans, D., and Coheur, P.-F.: Global ammonia distribution derived from infrared
698 satellite observations, *Nat. Geosci.*, 2, 479–483, <https://doi.org/10.1038/ngeo551>, 2009.

699 Clarisse, L., Shephard, M., Dentener, F., Hurtmans, D., CadyPereira, K., Karagulian, F., Van Damme, M., Clerbaux, C., and
700 Coheur, P.-F.: Satellite monitoring of ammonia: A case study of the San Joaquin Valley, *J. Geophys. Res.*, 115, D13302,
701 <https://doi.org/10.1029/2009JD013291>, 2010.

702 Clarisse, L., Van Damme, M., Coheur, P.-F., and Clerbaux, C.: Tracking down global NH₃ point sources with wind-adjusted
703 superresolution, *Atmos. Meas. Tech.*, 12, 5457–5473, <https://doi.org/10.5194/amt-12-5457-2019>, 2019.

704 Clarisse, L., Van Damme, M., Hurtmans, D., Franco, B., Clerbaux, C., and Coheur, P.-F.: The diel cycle of NH₃ observed from
705 the FY-4A Geostationary Interferometric Infrared Sounder (GIIRS), *Geophys. Res. Lett.*, 48, e2021GL093010,
706 <https://doi.org/10.1029/2021GL093010>, 2021.

707 Clarisse, L., Franco, B., Van Damme, M., Di Gioacchino, T., Hadji-Lazaro, J., Whitburn, S., Noppen, L., Hurtmans, D.,
708 Clerbaux, C., and Coheur, P.: The IASI NH₃ version 4 product: averaging kernels and improved consistency, *Atmos.*
709 *Meas. Tech.*, 16, 5009–5028, <https://doi.org/10.5194/amt-16-5009-2023>, 2023.

710 Clerbaux, C., Boynard, A., Clarisse, L., George, M., Hadji-Lazaro, J., Herbin, H., Hurtmans, D., Pommier, M., Razavi, A.,
711 Turquety, S., Wespes, C., and Coheur, P.-F.: Monitoring of atmospheric composition using the thermal infrared
712 IASI/MetOp sounder, *Atmos. Chem. Phys.*, 9, 6041–6054, <https://doi.org/10.5194/acp-9-6041-2009>, 2009.

713 Dammers, E., Schaap, M., Haaima, M., Palm, M., Wichink Kruit, R. J., van Zanten, M. C., and Erisman, J. W.: Measuring
714 atmospheric ammonia with remote sensing campaign: Part 1—characterisation of vertical ammonia concentration profile
715 in the centre of The Netherlands, *Atmos. Environ.*, 169, 97–112, <https://doi.org/10.1016/j.atmosenv.2017.08.067>, 2017a.

716 Dammers, E., Shephard, M. W., Palm, M., Cady-Pereira, K., Capps, S., Lutsch, E., Strong, K., Hannigan, J. W., Ortega, I.,
717 Toon, G. C., Stremme, W., Grutter, M., Jones, N., Smale, D., Siemons, J., Hrpcek, K., Tremblay, D., Schaap, M., Notholt,
718 J., and Erisman, J. W.: Validation of the CrIS fast physical NH₃ retrieval with ground-based FTIR, *Atmos. Meas. Tech.*,
719 10, 2645–2667, <https://doi.org/10.5194/amt-10-2645-2017>, 2017b.

720 Dammers, E., McLinden, C. A., Griffin, D., Shephard, M. W., Van Der Graaf, S., Lutsch, E., Schaap, M., Gainairu-Matz, Y.,
721 Fioletov, V., Van Damme, M., Whitburn, S., Clarisse, L., Cady-Pereira, K., Clerbaux, C., Coheur, P. F., and Erisman, J.
722 W.: NH₃ emissions from large point sources derived from CrIS and IASI satellite observations, *Atmos. Chem. Phys.*, 19,
723 12261–12293, <https://doi.org/10.5194/acp-19-12261-2019>, 2019.

724 Ding, Y., Ren, G., Li, Q., Sun, X., and Zhou, B.: High-impact extreme weather and climate events in China: summer 2024
725 overview, *Adv. Atmos. Sci.*, 41, 1123–1135, <https://doi.org/10.1007/s00376-024-4462-6>, 2024.

726 Gong, C., Tian, H., Liao, H., Pan, N., Pan, S., Ito, A., Jain, A. K., Kou-Giesbrecht, S., Joos, F., Sun, Q., Shi, H., Vuichard, N.,
727 Zhu, Q., Peng, C., Maggi, F., Tang, F. H. M., and Zaehle, S.: Global net climate effects of anthropogenic reactive nitrogen,
728 *Atmos. Chem. Phys.*, 24, 557–563, <https://doi.org/10.1038/s41586-024-07714-4>, 2024.

729 Gu, M., Pan, Y., Walters, W. W., Sun, Q., Song, L., Fang, Y., and Xue, Y.: Vehicular emissions enhanced ammonia
730 concentrations in winter mornings: insights from diurnal nitrogen isotopic signatures, *Environ. Sci. Technol.*, 56, 1578–
731 1585, <https://doi.org/10.1021/acs.est.1c05884>, 2022.

732 Guendouz, N., Viatte, C., Zeng, Z.-C., Boynard, A., Safieddine, S., Standfuss, C., Turquety, S., Van Damme, M., Clarisse, L.,
733 Coheur, P., Armante, R., Prunet, P., and Clerbaux, C.: Monitoring atmospheric ammonia from geostationary orbit:
734 contributions of GIIRS-B and IRS remote sensors, *ESS Open Archive* [preprint],
735 <https://doi.org/10.22541/essoar.175767134.49615241/v1>, September 12, 2025.

736 Guo, X., Clarisse, L., Wang, R., Van Damme, M., Whitburn, S., Coheur, P.-F., Clerbaux, C., Franco, B., Pan, D., Golston, L.
737 M., Wendt, L., Sun, K., Tao, L., Miller, D., Mikoviny, T., Müller, M., Wisthaler, A., Tevlin, A. G., Murphy, J. G., Nowak,
738 J. B., Roscioli, J. R., Volkamer, R., Kille, N., Neuman, J. A., Eilerman, S. J., Crawford, J. H., Yacovitch, T. I., Barrick,
739 J. D., Scarino, A. J., and Zondlo, M. A.: Validation of IASI satellite ammonia observations at the pixel scale using in-situ
740 vertical profiles, *J. Geophys. Res. Atmos.*, 126, e2020JD033475, <https://doi.org/10.1029/2020JD033475>, 2021.

741 He, Y., Pan, Y., Zhang, G., Ji, D., Tian, S., Xu, X., Zhang, R., and Wang, Y.: Tracking ammonia morning peak, sources and
742 transport with 1 Hz measurements at a rural site in North China Plain, *Atmos. Environ.*, 235, 117630,
743 <https://doi.org/10.1016/j.atmosenv.2020.117630>, 2020.

744 Hersbach, H., Bell, B., Berrisford, P., Biavati, G., Horányi, A., Muñoz Sabater, J., Nicolas, J., Peubey, C., Radu, R., Rozum,
745 I., Schepers, D., Simmons, A., Soci, C., Dee, D., and Thépaut, J.-N.: ERA5 hourly data on single levels from 1940 to

746 present. Copernicus Climate Change Service (C3S) Climate Data Store (CDS), <https://doi.org/10.24381/cds.adbb2d47>,
747 2023 (Accessed on 20-June-2025)

748 Holmlund, K., Grandell, J., Schmetz, J., Stuhlmann, R., Bojkov, B., Munro, R., Lekouara, M., Coppens, D., Viticchie, B.,
749 August, T., Theodore, B., Watts, P., Dobber, M., Fowler, G., Bojinski, S., Schmid, A., Salonen, K., Tjemkes, S., Aminou,
750 D., and Blythe, P.: Meteosat Third Generation (MTG): Continuation and innovation of observations from geostationary
751 orbit, *Bull. Amer. Meteor. Soc.*, 102, E990–E1015, <https://doi.org/10.1175/BAMS-D-19-0304.1>, 2021.

752 Hou, X. and Yu, X.: An ammonia emissions inventory for agricultural sources in Hefei, China, *Atmos. Ocean. Sci. Lett.*, 13
753 (3), 260–267, <https://doi.org/10.1080/16742834.2020.1747355>, 2020.

754 Hua, J., Zhou, R., Sheng, M., and Zeng, Z.-C.: Global and diurnal variations in tropospheric ammonia observed from a
755 constellation of hyperspectral infrared sounders in three different LEO orbits, *EGUsphere* [preprint],
756 <https://doi.org/10.5194/egusphere-2026-746>, 2026.

757 Huy, D. H., Thanh, L. T., Hien, T. T., Takenaka, N., and Huy, D. H.: Characteristics of ammonia gas and fine particulate
758 ammonium from two distinct urban areas: Osaka, Japan, and Ho Chi Minh City, Vietnam, *Environ. Sci. Pollut. Res.*, 24,
759 8147–8163, <https://doi.org/10.1007/s11356-017-8496-5>, 2017.

760 Jang, J.-H., Hong, J., Kim, J. B., Park, S., Hwang, K., Kim, J., Kim, J. Y., Bae, G.-N., Kim, S., and Kim, K. H.: Influence of
761 atmospheric ammonia on secondary inorganic aerosol formation in PM_{2.5} during spring 2024 in the Hongseong area,
762 Republic of Korea, *Atmos. Environ.*, 358, 121363, <https://doi.org/10.1016/j.atmosenv.2025.121363>, 2025.

763 Jongenelen, T., van Zanten, M., Dammers, E., Wichink Kruit, R., Hensen, A., Geers, L., and Erisman, J. W.: Validation and
764 uncertainty quantification of three state-of-the-art ammonia surface exchange schemes using NH₃ flux measurements in
765 a dune ecosystem, *Atmos. Chem. Phys.*, 25, 4943–4963, <https://doi.org/10.5194/acp-25-4943-2025>, 2025.

766 Kang, Y., Liu, M., Song, Y., Huang, X., Yao, H., Cai, X., Zhang, H., Kang, L., Liu, X., Yan, X., He, H., Zhang, Q., Shao, M.,
767 and Zhu, T.: High-resolution ammonia emissions inventories in China from 1980 to 2012, *Atmos. Chem. Phys.*, 16, 2043–
768 2058, <https://doi.org/10.5194/acp-16-2043-2016>, 2016.

769 Keller, C.-A., Knowland, K.-E., Duncan, B.-N., Liu, J., Anderson, D.-C., Das, S., Lucchesi, R.-A., Lundgren, E.-W., Nicely,
770 J.-M., Nielsen, E., Ott, L.-E., Saunders, E., Strode, S.-A., Wales, P.-A., Jacob, D.-J., and Pawson, S.: Description of the
771 NASA GEOS composition forecast modeling system GEOS-CF v1.0, *J. Adv. Model. Earth Syst.*, 13, e2020MS002413,
772 <https://doi.org/10.1029/2020MS002413>, 2021.

773 Kharol, S. K., Shephard, M. W., McLinden, C. A., Zhang, L., Sioris, C. E., O'Brien, J. M., Hakami, A., Murphy, J. G., van
774 Donkelaar, A., and Martin, R. V.: Dry deposition of reactive nitrogen from satellite observations of ammonia and nitrogen
775 dioxide over North America, *Geophys. Res. Lett.*, 45, 1157–1166, <https://doi.org/10.1002/2017GL076772>, 2018.

776 Kim, J., Jeong, U., Ahn, M. H., Kim, J. H., Park, R. J., Lee, H., Song, C. H., Choi, Y. S., Lee, K. H., Yoo, J. M., Jeong, M. J.,
777 Park, S. K., Lee, K. M., Song, C. K., Kim, S. W., Kim, Y. J., Kim, S. W., Kim, M., Go, S., Liu, X., Chance, K., Miller,
778 C. C., Al-Saadi, J., Veihelmann, B., Bhartia, P. K., Torres, O., Abad, G. G., Haffner, D. P., Ko, D. H., Lee, S. H., Woo,
779 J. H., Chong, H., Park, S. S., Nicks, D., Choi, W. J., Moon, K. J., Cho, A., Yoon, J., Kim, S. kyun, Hong, H., Lee, K.,

780 Lee, H., Lee, S., Choi, M., Veeffkind, P., Levelt, P. F., Edwards, D. P., Kang, M., Eo, M., Bak, J., Baek, K., Kwon, H. A.,
781 Yang, J., Park, J., Han, K. M., Kim, B. R., Shin, H. W., Choi, H., Lee, E., Chong, J., Cha, Y., Koo, J. H., Irie, H.,
782 Hayashida, S., Kasai, Y., Kanaya, Y., Liu, C., Lin, J., Crawford, J. H., Carmichael, G. R., Newchurch, M. J., Lefter, B. L.,
783 Herman, J. R., Swap, R. J., Lau, A. K. H., Kurosu, T. P., Jaross, G., Ahlers, B., Dobber, M., McElroy, C. T. and Choi, Y.:
784 New era of air quality monitoring from space: Geostationary environment monitoring spectrometer (GEMS), *B. Am.*
785 *Meteorol. Soc.*, 101, E1–E22, <https://doi.org/10.1175/BAMS-D-18-0013.1>, 2020.

786 Kumar, P., Broquet, G., Hauglustaine, D., Beaudor, M., Clarisse, L., Van Damme, M., Coheur, P., Cozic, A., Zheng, B.,
787 Revilla Romero, B., Delavois, A., and Ciais, P.: Global atmospheric inversion of the anthropogenic NH₃ emissions over
788 2019–2022 using the LMDZ-INCA chemistry transport model and the IASI NH₃ observations, *Atmos. Chem. Phys.*, 25,
789 12379–12407, <https://doi.org/10.5194/acp-25-12379-2025>, 2025.

790 Lan, Z., Lin, W., and Zhao, G.: Sources, variations, and effects on air quality of atmospheric ammonia, *Curr. Pollut. Rep.*, 10,
791 40–53, <https://doi.org/10.1007/s40726-023-00291-6>, 2024.

792 Li, B., Chen, L., Shen, W., Jin, J., Wang, T., Wang, P., Yang, Y., and Liao, H.: Improved gridded ammonia emission inventory
793 in China, *Atmos. Chem. Phys.*, 21, 15883–15900, <https://doi.org/10.5194/acp-21-15883-2021>, 2021.

794 Li, M., Kurokawa, J., Zhang, Q., Woo, J.-H., Morikawa, T., Chatani, S., Lu, Z., Song, Y., Geng, G., Hu, H., Kim, J., Cooper,
795 O. R., and McDonald, B. C.: MIXv2: a long-term mosaic emission inventory for Asia (2010–2017), *Atmos. Chem. Phys.*,
796 24, 3925–3952, <https://doi.org/10.5194/acp-24-3925-2024>, 2024.

797 Li, Z., Sun, K., Guan, K., Wang, S., Peng, B., Clarisse, L., Van Damme, M., Coheur, P.-F., Cady-Pereira, K., Shephard, M.
798 W., Zondlo, M., and Moore, D.: Ammonia emissions and depositions over the contiguous United States derived from
799 IASI and CrIS using the directional derivative approach, *Atmos. Chem. Phys.*, 26, 703–721, <https://doi.org/10.5194/acp-26-703-2026>, 2026.

800

801 Lin, Y.-C., Zhang, Y.-L., Fan, M.-Y., and Bao, M.: Heterogeneous formation of particulate nitrate under ammonium-rich
802 regimes during the high-PM_{2.5} events in Nanjing, China, *Atmos. Chem. Phys.*, 20, 3999–4011,
803 <https://doi.org/10.5194/acp-20-3999-2020>, 2020.

804 Liu, L., Zhang, X., Wong, A. Y. H., Xu, W., Liu, X., Li, Y., Mi, H., Lu, X., Zhao, L., Wang, Z., Wu, X., and Wei, J.: Estimating
805 global surface ammonia concentrations inferred from satellite retrievals, *Atmos. Chem. Phys.*, 19, 12051–12066,
806 <https://doi.org/10.5194/acp-19-12051-2019>, 2019.

807 Luo, X., Zhang, M., Ni, Y., and Shen, G.: Mitigation strategies for NH₃ and N₂O emissions in greenhouse agriculture: Insights
808 into fertilizer management and nitrogen emission mechanisms, *Environ. Technol. Innov.*, 37, 103995,
809 <https://doi.org/10.1016/j.eti.2024.103995>, 2025.

810 Luo, Z., Zhang, Y., Chen, W., Van Damme, M., Coheur, P.-F., and Clarisse, L.: Estimating global ammonia (NH₃) emissions
811 based on IASI observations from 2008 to 2018, *Atmos. Chem. Phys.*, 22, 10375–10388, [https://doi.org/10.5194/acp-22-](https://doi.org/10.5194/acp-22-10375-2022)
812 10375-2022, 2022.

813 Marais, E. A., Pandey, A. K., Van Damme, M., Clarisse, L., Coheur, P.-F., Shephard, M. W., Cady-Pereira, K. E., Misselbrook,
814 T., Zhu, L., Luo, G., and Yu, F.: UK ammonia emissions estimated with satellite observations and GEOS-Chem, *J.*
815 *Geophys. Res. Atmos.*, 126, e2021JD035237, <https://doi.org/10.1029/2021JD035237>, 2021.

816 Meng, Z. Y., Lin, W. L., Jiang, X. M., Yan, P., Wang, Y., Zhang, Y. M., Jia, X. F., and Yu, X. L.: Characteristics of atmospheric
817 ammonia over Beijing, China, *Atmos. Chem. Phys.*, 11, 6139–6151, <https://doi.org/10.5194/acp-11-6139-2011>, 2011.

818 Meng, Z., Xu, X., Lin, W., Ge, B., Xie, Y., Song, B., Jia, S., Zhang, R., Peng, W., Wang, Y., Cheng, H., Yang, W., and Zhao,
819 H.: Role of ambient ammonia in particulate ammonium formation at a rural site in the North China Plain, *Atmos. Chem.*
820 *Phys.*, 18, 167–184, <https://doi.org/10.5194/acp-18-167-2018>, 2018.

821 Pai, S. J., Heald, C. L., and Murphy, J. G.: Exploring the global importance of atmospheric ammonia oxidation, *ACS Earth*
822 *Space Chem.*, 5, 1674–1685, <https://doi.org/10.1021/acsearthspacechem.1c00021>, 2021.

823 Pawar, P. V., Ghude, S. D., Jena, C., Móríng, A., Sutton, M. A., Kulkarni, S., Lal, D. M., Surendran, D., Van Damme, M.,
824 Clarisse, L., Coheur, P.-F., Liu, X., Govardhan, G., Xu, W., Jiang, J., and Adhya, T. K.: Analysis of atmospheric ammonia
825 over South and East Asia based on the MOZART-4 model and its comparison with satellite and surface observations,
826 *Atmos. Chem. Phys.*, 21, 6389–6409, <https://doi.org/10.5194/acp-21-6389-2021>, 2021.

827 Saraswati, G. M. P., Sharma, S. K., Mandal, T. K., Kotnala, R. K.: Simultaneous measurements of ambient NH₃ and its
828 relationship with other trace gases, PM_{2.5} and meteorological parameters over Delhi, India, *MAPAN*, 34, 55–69,
829 <https://doi.org/10.1007/s12647-018-0286-0>, 2019.

830 Seinfeld, J. H. and Pandis, S. N.: *Atmospheric chemistry and physics: from air pollution to climate change*, 3rd edn., Wiley,
831 Hoboken, NJ, 1152 pp., ISBN 978-1-118-94740-1, 2016.

832 Shephard, M. W., Cady-Pereira, K. E., Luo, M., Henze, D. K., Pinder, R. W., Walker, J. T., Rinsland, C. P., Bash, J. O., Zhu,
833 L., Payne, V. H., and Clarisse, L.: TES ammonia retrieval strategy and global observations of the spatial and seasonal
834 variability of ammonia, *Atmos. Chem. Phys.*, 11, 10743–10763, <https://doi.org/10.5194/acp-11-10743-2011>, 2011.

835 Shephard, M. W. and Cady-Pereira, K. E.: Cross-track Infrared Sounder (CrIS) satellite observations of tropospheric ammonia,
836 *Atmos. Meas. Tech.*, 8, 1323–1336, <https://doi.org/10.5194/amt-8-1323-2015>, 2015.

837 Shephard, M. W., Dammers, E., Cady-Pereira, K. E., Kharol, S. K., Thompson, J., Gainariu-Matz, Y., Zhang, J., McLinden,
838 C. A., Kovachik, A., Moran, M., Bittman, S., Sioris, C. E., Griffin, D., Alvarado, M. J., Lonsdale, C., Savic-Jovicic, V.,
839 and Zheng, Q.: Ammonia measurements from space with the Cross-track Infrared Sounder: characteristics and
840 applications, *Atmos. Chem. Phys.*, 20, 2277–2302, <https://doi.org/10.5194/acp-20-2277-2020>, 2020.

841 Shephard, M. W., Kharol, S. K., Dammers, E., Sioris, C. E., Bell, A., Jansen, R., Caron, J., Snel, R., Palombo, E., Cady-Pereira,
842 K. E., McLinden, C. A., Lutsch, E., and Knuteson, R.: Infrared satellite detection limits for monitoring atmospheric
843 ammonia, *IEEE J. Sel. Top. Appl. Earth Obs. Remote Sens.*, 18, 10271–10291,
844 <https://doi.org/10.1109/JSTARS.2025.3557240>, 2025.

845 Teng, X., Hu, Q., Zhang, L., Qi, J., Shi, J., Xie, H., Gao, H., and Yao, X.: Identification of major sources of atmospheric NH₃
846 in an urban environment in northern China during wintertime, *Environ. Sci. Technol.*, 51, 6839–6848, [https://doi.org/](https://doi.org/10.1021/acs.est.7b00328)
847 10.1021/acs.est.7b00328, 2017.

848 Vadrevu, K. P., Lasko, K., Giglio, L., Schroeder, W., Biswas, S., and Justice, C.: Trends in Vegetation fires in South and
849 Southeast Asian Countries, *Sci. Rep.*, 9, 7422, <https://doi.org/10.1038/s41598-019-43940-x>, 2019.

850 Van Damme, M., Erisman, J. W., Clarisse, L., Dammers, E., Whitburn, S., Clerbaux, C., Dolman, A. J., and Coheur, P.-F.:
851 Worldwide spatiotemporal atmospheric ammonia (NH₃) columns variability revealed by satellite, *Geophys. Res. Lett.*,
852 42, 8660–8668, <https://doi.org/10.1002/2015GL065496>, 2015.

853 Van Damme, M., Clarisse, L., Whitburn, S., Hadji-Lazaro, J., Hurtmans, D., Clerbaux, C., and Coheur, P.-F.: Industrial and
854 agricultural ammonia point sources exposed, *Nature*, 564, 99–103, <https://doi.org/10.1038/s41586-018-0747-1>, 2018.

855 Van Damme, M., Clarisse, L., Franco, B., Sutton, M. A., Erisman, J. W., Wichink Kruit, R., van Zanten, M., Whitburn, S.,
856 Hadji-Lazaro, J., and Hurtmans, D.: Global, regional and national trends of atmospheric ammonia derived from a decadal
857 (2008–2018) satellite record, *Environ. Res. Lett.*, 16, 055017, <https://doi.org/10.1088/1748-9326/abd5e0>, 2021.

858 Wang, S., Nan, J., Shi, C., Fu, Q., Gao, S., Wang, D., Cui, H., Saiz-Lopez, A., and Zhou, B.: Atmospheric ammonia and its
859 impacts on regional air quality over the megacity of Shanghai, China, *Sci. Rep.-UK*, 5, 15842,
860 <https://doi.org/10.1038/srep15842>, 2015.

861 Wang, W., Tian, Y., Liu, C., Sun, Y., Liu, W., Xie, P., Liu, J., Xu, J., Morino, I., Velazco, V. A., Griffith, D. W. T., Notholt,
862 J., and Warneke, T.: Investigating the performance of a greenhouse gas observatory in Hefei, China, *Atmos. Meas. Tech.*,
863 10, 2627–2643, <https://doi.org/10.5194/amt-10-2627-2017>, 2017.

864 Wang, W., Liu, C., Clarisse, L., Van Damme, M., Coheur, P.-F., Xie, Y., Shan, C., Hu, Q., Sun, Y., and Jones, N.: Ground-
865 based measurements of atmospheric NH₃ by Fourier transform infrared spectrometry at Hefei and comparisons with IASI
866 data, *Atmos. Environ.*, 287, 119256, <https://doi.org/10.1016/j.atmosenv.2022.119256>, 2022.

867 Warner, J. X., Wei, Z., Strow, L. L., Dickerson, R. R., and Nowak, J. B.: The global tropospheric ammonia distribution as seen
868 in the 13-year AIRS measurement record, *Atmos. Chem. Phys.*, 16, 5467–5479, [https://doi.org/10.5194/acp-16-5467-](https://doi.org/10.5194/acp-16-5467-2016)
869 2016, 2016.

870 White, E., Shephard, M. W., Cady-Pereira, K. E., Kharol, S., Ford, S., Dammers, E., Chow, E., Thiessen, N., Tobin, D., Quinn,
871 G., O'Brien, J., and Bash, J.: Accounting for non-detects in satellite retrievals: application using CrIS ammonia
872 observations, *Remote Sens.*, 15, 2610, <https://doi.org/10.3390/rs15102610>, 2023.

873 Whitburn, S., Van Damme, M., Clarisse, L., Bauduin, S., Heald, C. L., Hadji-Lazaro, J., Hurtmans, D., Zondlo, M. A., Clerbaux,
874 C., and Coheur, P.-F.: A flexible and robust neural network IASI-NH₃ retrieval algorithm, *J. Geophys. Res.-Atmos.*, 121,
875 6581–6599, <https://doi.org/10.1002/2016JD024828>, 2016.

876 Wunch, D., G. C. Toon, J.-F. L. Blavier, R. A. Washenfelder, J. Notholt, B. J. Connor, D. W. T. Griffith, V. Sherlock, and P.
877 O. Wennberg: The Total Carbon Column Observing Network, *Philos. Trans. R. Soc. A Math. Phys. Eng. Sci.*, 369(1943),
878 2087–2112, <https://doi.org/10.1098/rsta.2010.0240>, 2011.

879 Xu, J., Lu, M., Guo, Y., Zhang, L., Chen, Y., Liu, Z., Zhou, M., Lin, W., Pu, W., Ma, Z., Song, Y., Pan, Y., Liu, L., and Ji, D.:
880 Summertime urban ammonia emissions may be substantially underestimated in Beijing, China, *Environ. Sci. Technol.*,
881 57, 13124–13135, <https://doi.org/10.1021/acs.est.3c05266>, 2023.

882 Yang, J., Zhang, Z., Wei, C., Lu, F., and Guo, Q.: Introducing the new generation of Chinese geostationary weather satellites,
883 Fengyun-4B. *Am. Meteorol. Soc.*, 98, 1637–1658, <https://doi.org/10.1175/BAMS-D-16-0065.1>, 2017.

884 Yang, X., He, J., and Wang, S.: Interannual variability of atmospheric ammonia over the Sichuan Basin, southwestern China:
885 Trend, sources, and implications on particle matter control, *Atmos. Chem. Phys.*, 299, 107170,
886 <https://doi.org/10.1016/j.atmosres.2023.107170>, 2024.

887 Zeng, Z.-C., Lee, L., Qi, C., Clarisse, L., and Van Damme, M.: Optimal estimation retrieval of tropospheric ammonia from
888 the Geostationary Interferometric Infrared Sounder on board FengYun-4B, *Atmos. Meas. Tech.*, 16, 3693–3713,
889 <https://doi.org/10.5194/amt-16-3693-2023>, 2023a.

890 Zeng, Z.-C., Lee, L., and Qi, C.: Diurnal carbon monoxide observed from a geostationary infrared hyperspectral sounder: first
891 result from GIIRS on board FengYun-4B, *Atmos. Meas. Tech.*, 16, 3059–3083, [https://doi.org/10.5194/amt-16-3059-](https://doi.org/10.5194/amt-16-3059-2023)
892 2023, 2023b.

893 Zeng, Z.-C. FengYun-4B/GIIRS FYGeoAIR NH₃ retrievals from July 2022 to June 2025 [Data set]. Zenodo.
894 <https://doi.org/10.5281/zenodo.17193848>, 2025.

895 Zhang, L., Chen, Y., Zhao, Y., Henze, D. K., Zhu, L., Song, Y., Paulot, F., Liu, X., Pan, Y., Lin, Y., and Huang, B.: Agricultural
896 ammonia emissions in China: reconciling bottom-up and top-down estimates, *Atmos. Chem. Phys.*, 18, 339–355,
897 <https://doi.org/10.5194/acp-18-339-2018>, 2018.

898 Zhang, Q., Pan, Y., He, Y., Zhao, Y., Zhu, L., Zhang, X., Xu, X., Ji, D., Gao, J., Tian, S., Gao, W., and Wang, Y.: Bias in
899 ammonia emission inventory and implications on emission control of nitrogen oxides over North China Plain,
900 *Atmospheric Environment*, 214, 116869, <https://doi.org/10.1016/j.atmosenv.2019.116869>, 2019.

901 Zhou, X., Li, Y., Xiao, C., Chen, W., Mei, M., and Wang, G.: High-impact extreme weather and climate events in China:
902 summer 2024 overview, *Adv. Atmos. Sci.*, 42, 1064–1076, <https://doi.org/10.1007/s00376-024-4462-6>, 2025.